



A Modeling Study of the Seasonal, Latitudinal, and Temporal Distribution of the Meteoroid Mass Input at Mars: Constraining the Deposition of Meteoric Ablated Metals in the Upper Atmosphere

Juan Diego Carrillo-Sánchez^{1,2} , Diego Janches² , John M. C. Plane³ , Petr Pokorný^{1,4,5} , Menelaos Sarantos⁶ ,
Matteo M. J. Crismani⁷ , Wuhu Feng^{3,8} , and Daniel R. Marsh^{9,10}

¹ Department of Physics, Catholic University of America, 620 Michigan Avenue N.E., Washington, DC 20064, USA; juandiego.carrillosanchez@nasa.gov

² ITM Physics Laboratory, NASA/Goddard Space Flight Center, Code 675, 8800 Greenbelt Road, Greenbelt, MD 20771, USA

³ School of Chemistry, University of Leeds, Woodhouse Lane, Leeds LS2 9JT, UK

⁴ Astrophysics Science Division, NASA/Goddard Space Flight Center, Code 667, 8800 Greenbelt Road, Greenbelt, MD 20771, USA

⁵ Center for Research and Exploration in Space Science and Technology, NASA/GSFC, 8800 Greenbelt Road, MD 20771, USA

⁶ Geospace Physics Laboratory, NASA/Goddard Space Flight Center, Code 673, 8800 Greenbelt Road, Greenbelt, MD 20771, USA

⁷ California State University, San Bernardino, Department of Physics, 5500 University Parkway, San Bernardino, CA 92407, USA

⁸ National Centre for Atmospheric Science, University of Leeds, Woodhouse Lane, Leeds, LS2 9PH, UK

⁹ National Center for Atmospheric Research, 1850 Table Mesa Drive, Boulder, CO 80305, USA

¹⁰ School of Physics and Astronomy, University of Leeds, Woodhouse Lane, Leeds LS2 3AR, UK

Received 2022 April 11; revised 2022 July 15; accepted 2022 July 27; published 2022 October 21

Abstract

This study provides a comprehensive description of the deposition of meteor-ablated metals in the upper atmosphere of Mars, accounting for the temporal, vertical, latitudinal, and seasonal distribution. For this purpose, the Leeds Chemical Ablation Model is combined with a meteoroid input function to characterize the size and velocity distributions of three distinctive meteoroid populations around Mars—the Jupiter-family comets (JFCs), main-belt asteroids, and Halley-type comets (HTCs). These modeling results show a significant midnight-to-noon enhancement of the total mass influx because of the orbital dynamics of Mars, with meteoroid impacts preferentially distributed around the equator for particles with diameters below 2000 μm . The maximum total mass input occurs between the northern winter and the first crossing of the ecliptic plane with 2.30 tons sol^{-1} , with the JFCs being the main contributor to the overall influx with up to 56% around Mars' equator. Similarly, total ablated atoms mainly arise from the HTCs with a maximum injection rate of 0.71 tons sol^{-1} spanning from perihelion to the northern winter. In contrast, the minimum mass and ablated inputs occur between the maximum vertical distance above the ecliptic plane and aphelion with 1.50 and 0.42 tons sol^{-1} , respectively. Meteoric ablation occurs approximately in the range altitude between 100 and 60 km with a strong midnight-to-noon enhancement at equatorial latitudes. The eccentricity and the inclination of Mars' orbit produces a significant shift of the ablation peak altitude at high latitudes as Mars moves toward, or away, from the northern/southern solstices.

Unified Astronomy Thesaurus concepts: [Zodiacal cloud \(1845\)](#); [Comets \(280\)](#); [Short period comets \(1452\)](#); [Long period comets \(933\)](#); [Asteroid belt \(70\)](#); [Meteoroids \(1040\)](#); [Meteors \(1041\)](#); [Meteor radiants \(1033\)](#); [Micrometeorites \(1047\)](#); [Meteorite composition \(1037\)](#); [Mars \(1007\)](#); [Planetary atmospheres \(1244\)](#)

Supporting material: animations

1. Introduction

The inner solar system is populated by interplanetary dust particles (IDPs) released from cometary trails and collisions between asteroids (Cepelcha et al. 1998). Planetary bodies and satellites therefore encounter a cloud of IDPs along their orbits, giving rise to a permanent bombardment on their respective atmospheres or surfaces (Plane et al. 2018a; Janches et al. 2020). Constraining the magnitude of the mass influx of IDPs onto a solar system body is crucial for understanding the effects in their atmospheres and on their surfaces.

Most IDPs impacting terrestrial planets are stony chondrites consisting of Carbonaceous Ivuna (CI)- and Carbonaceous Mighei (CM)-like fine-grained aggregates containing a variety of anhydrous and hydrated silicate minerals, along with troilite (FeS) and Fe–Ni alloys (Taylor et al. 2012). For planetary bodies with

atmospheres, collisions with air molecules lead to the thermal ablation of IDPs above their melting temperature (Vondrak et al. 2008; Carrillo-Sánchez et al. 2015) and, therefore, their constituent elements evaporate and produce layers of free neutral and ionized atoms (Plane 2003; Plane et al. 2015, 2018b). Mg, Fe, Si, and Na are the major metallic species in the Earth's upper atmosphere, while K and Ca are present at least one order of magnitude lower in concentration (Plane 2003). Metallic layers in the Earth's atmosphere have been widely studied for decades using ground-based light detection and ranging (LiDAR) and space-based optical spectroscopy. These observations show that Mg^+ and Fe^+ are the metallic constituents of the lower E region (Plane et al. 2015). Metal atoms may experience collisional ionization during thermal ablation, and can also be subsequently ionized by photoionization and charge transfer reactions with major ionospheric ions such as NO^+ and O_2^+ on Earth (Plane 2003; Plane et al. 2015), and O_2^+ on Mars (Whalley & Plane 2010).

Recently, the Mars Atmosphere and Volatile Evolution (MAVEN) Imaging Ultraviolet Spectrograph (IUVS) reported the first detection of a persistent Mg^+ layer in Mars' atmosphere



Original content from this work may be used under the terms of the [Creative Commons Attribution 4.0 licence](#). Any further distribution of this work must maintain attribution to the author(s) and the title of the work, journal citation and DOI.

peaking around 90 km (Crismani et al. 2017). Schneider et al. (2015), Benna et al. (2015), and Crismani et al. (2018) reported the detection of metallic ion layers in the aftermath of the meteor storm created by the close encounter of Comet Siding Spring (C/2013 A1) and Mars. In addition, Grebowsky et al. (2017) detected a range of metallic ions using the Neutral Gas Ion Mass Spectrometer (NGIMS) on MAVEN during deep-dip orbits down to ~ 130 km. Furthermore, Crismani et al. (2022) recently reported seven Earth years of MAVEN/IUVS observations of the sporadic background of Mg^+ at Mars. These measurements demonstrate that Mg^+ is a dynamic layer that exhibits a strong equatorial dawnside enhancement and a significant shift of the altitude of the Mg^+ peak seasonally.

Several atmospheric studies of Mars have explored in detail the distribution and chemistry of meteoric metal layers in the Martian aerobraking region around 90 km (Pesnell & Grebowsky 2000; Molina-Cuberos et al. 2003; Whalley & Plane 2010; Plane et al. 2018b). More recently, Carrillo-Sánchez et al. (2020a, 2020b) combined the zodiacal cloud model (ZCM) and the Chemical Ablation MODel (CABMOD) to describe the injection rate profiles of the main meteoric chemical species into the atmospheres of Earth, Mars, and Venus, and to constrain the contributions of three cosmic dust sources: Jupiter-family comets (JFCs), main-belt asteroids (ASTs), and Halley-type comets (HTCs). The CABMOD-ZCM model made several assumptions to determine the contribution of the three cosmic dust sources:

1. The meteoroid mass and velocity distributions are uniform throughout the orbit's planet.
2. The radiant distributions of meteoroids in ecliptic coordinates are also assumed constant with orbital position, and they are then converted into the corresponding planet-fixed coordinates to estimate the entry angle of any particle at a latitude of 40°N for Mars.
3. The CABMOD model used the Mars Climate Database (MCD; http://www-Mars.lmd.jussieu.fr/mcd_python/; Lewis et al. 1999), which summarizes the main features of the atmospheric structure and chemical composition estimated by the Mars Laboratoire de Météorologie Dynamique (LMD) model, to simulate the atmospheric density profile for the specific conditions of northern winter at 40°N and assumed that this description is constant both latitudinally and seasonally.
4. The ablation rates of meteoric metals estimated for these local conditions are then extrapolated globally removing any diurnal, spatial, or orbital variability.

In summary, Carrillo-Sánchez et al. (2020a, 2020b) estimated that the global mass flux into the Martian atmosphere is 2.2 ± 1.2 tons sol^{-1} , with contributions from JFCs, ASTs, and HTCs of 52%, 14%, and 34%, respectively. JFCs were the main mass contributor to the total accreted mass, consistent with previous estimates (Zook 2001; Nesvorný et al. 2010; Rowan-Robinson & May 2013; Yang & Ishiguro 2015) and with most of the incoming mass surviving as unmelted micrometeorites.

In the present study, we aim to address the limitations of the CABMOD-ZCM model and develop a comprehensive model to fully describe the temporal, vertical, spatial, and orbital variability of the injection rates of 10 meteoric chemical species—Si, Mg, Fe, Al, Ca, Ti, P, Na, K, and Ni—in the Martian atmosphere. For this purpose, we will combine the meteoroid input function (MIF) that characterizes for the first time the

diurnal, latitudinal, and seasonal distribution of incoming meteoroids on a planetary body (Janches et al. 2020), with the most recent version of the CABMOD model (Carrillo-Sánchez et al. 2020b).

2. Modeling the Seasonal, Latitudinal, and Temporal Variability of Meteoric Ablated Metals in the Martian Upper Atmosphere

Figure 1 illustrates a simplified diagram of the variability of the overall mass influx and the total ablated mass with the orbital position, defined by the solar longitude (L_s). This figure summarizes some of the results that are discussed in more detail in the following Sections. Note that most of the Figures in the present manuscript show a comparison of the corresponding results for three orbital positions: aphelion ($L_s = 71^\circ$, minimum total mass input), perihelion ($L_s = 251^\circ$, maximum deposition rates of meteoric metals), and first crossing of the ecliptic plane ($L_s = 325^\circ$, maximum mass influx for JFCs and ASTs). Figure 1 also shows the vertical distance of Mars (in astronomical unit) relative to the ecliptic plane (highlighted in yellow) as a function of the orbital position (see also Table 3 in Janches et al. 2020).¹¹

2.1. State-of-the-art Dynamical Models of the Zodiacal Cloud of Meteoroid Populations at Mars

The Dynamical Model of the Zodiacal Cloud (DMZC) describes the dynamical evolution of four meteoroid populations in the sporadic background around Mars' orbit (Pokorný et al. 2017, 2018, 2019), and it provides high-resolution maps of the mass flux and the entry velocities as a function of the orbital position and directions of arrival for the main meteoroid populations of the sporadic environment: the JFCs, ASTs, HTCs, and the Oort-Cloud comets (OCCs). The DMZC does not account for the potential contribution of meteor showers in the inner region because, even though they may increase the concentration of ablated atoms by a factor of two to three during a discrete time period for a given orbital position (Kopp 1997; Grebowsky et al. 1998), these meteor streams only represent $<10\%$ of the overall flux observed by radars on Earth (Brown et al. 2008). Recently, the Langmuir Probe and Waves (LPW) instrument on board the MAVEN spacecraft was able to detect for the first time the impact of IDPs in the narrow diameter range from 2–24 μm (Andersson et al. 2015), although the subsequent analyzes could not elucidate the origin of the measured dust. Likewise, the Juno spacecraft was launched in 2011 August and reached the Jupiter orbit insertion on 2016 July 4, in a trajectory that passed through the asteroid belt (Bolton et al. 2017). Despite not being instrumented with a dedicated dust detection instrument, the Juno spacecraft is equipped with an array of solar panels— ~ 60 m^2 aperture—combined with the Advance Stellar Compass, which is a complex system with four star-cameras that can be configured to search for nonstellar objects, such as asteroids (Connerney et al. 2017). Jorgensen et al. (2021) identified 15,278 impacts during 5 yr, and the Juno observations suggest that the largest impact rates of IDPs occur between the Earth aphelion and the 4:1 resonance with Jupiter— ~ 1.02 and ~ 2.065 au, respectively—at low inclination to the ecliptic plane. Additionally, according to their fitting model, the variation of zodiacal dust

¹¹ Note that there is a typo in Table 3 in Janches et al. (2020): the values of the ecliptic altitudes for perihelion and aphelion are swapped.

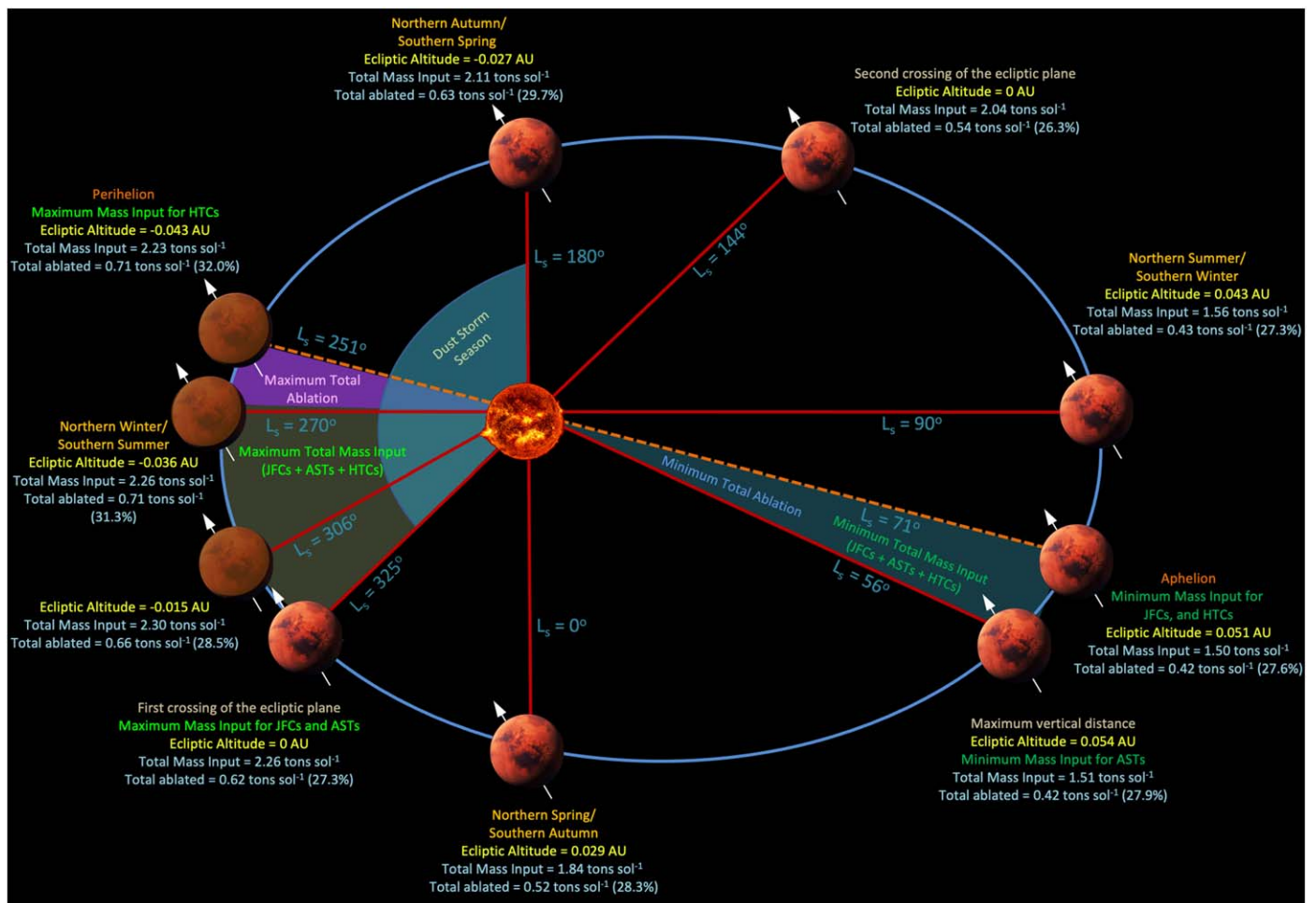


Figure 1. Diagram illustrating the variability of the total mass influx and the total ablated mass with the orbital position (L_s). The maximum global mass input occurs between $L_s = 270^\circ$ (northern winter/southern summer) and $L_s = 325^\circ$ (first crossing of the ecliptic plane), whereas the maximum deposition of metals in the Martian atmosphere matches with the maximum mass input of HTC at perihelion ($L_s = 251^\circ$). Note that the mass fluxes are expressed in tons sol⁻¹ (1 solar day at Mars is equivalent to 1.0275 Earth days). The values in parenthesis represent the fraction ablated with respect to the total mass input.

bands might be primarily explained by an unidentified single source with the initial inclination and orbital elements of Mars rather than the combined contribution of different meteoroid populations from cometary and asteroidal origin (as modeled by Carrillo-Sánchez et al. 2020a). Nonetheless, Pokorný et al. (2022) used the DMZC model to explain the Juno observations and concluded that: (1) the impact rates and the fluctuations of the dust flux with time modeled by the DMZC for the major meteoroid populations in the inner solar system are not consistent with the Juno observations during the cruise phase; (2) a hypothetical population of meteoroids arising from the Martian Hill Sphere—Mars itself or one of its moons—is not capable of replicating the events reported by Jorgensen et al. (2021); and (3) the impact rates can only be characterized by assuming a theoretical population of meteoroids with a contribution increasing with heliocentric distance, contrary to the current observations of the Zodiacal Cloud (Ade et al. 2014). Therefore, given the difficulty of replicating the Juno events through current dynamical models of meteoroids (Pokorný et al. (2022), in the present manuscript, we assume that the inner solar system is fundamentally populated by cometary dust and asteroids. Finally, in the case of meteoroids from the Edgeworth–Kuiper Belt (EKB) Object, the DMZC considers that their contribution to the overall flux in the inner

solar system is negligible (Poppe 2016), being two orders of magnitude lower than the corresponding flux of the JFCs. Modeling results based on the New Horizons Student Dust Counter observations of IDPs with diameters below 1000 μm (Poppe et al. 2019) indicate that $\sim 99\%$ of the solar system’s dust disk mass is contained in the outer solar system within the EKB and the OCCs located between 35 and 50 au, whereas the JFCs are the dominant source in the inner solar system, within 5 au, with the remaining $\sim 1\%$. However, most recently, Keller & Flynn (2022) analyzed the exposure ages of track-rich IDPs to solar energetic particles using a transmission electron microscope, concluding that track-rich IDPs have long exposure ages (>1 Myr), which excludes an origin from the JFCs and ASTs that exhibits space exposures of one or two orders of magnitude lower. Likewise, Keller & Flynn (2022) concluded that high track densities observed in $\sim 25\%$ of all IDPs suggest that they probably originated from the EKB. Consequently, future observations and modeling efforts are necessary to constrain the orbital parameters of the EKB meteoroids and their contribution to the overall flux in the inner solar system, even though it is rather likely that both their radiant and velocity distributions show similar features as the JFCs and/or the ASTs given their evolved dynamics.

In terms of size distribution, the DMZC considers meteoroid diameters between 10 and 2000 μm (Nesvorný et al. 2010, 2011). The DMZC model characterizes the impact probability of meteoroids with planetary bodies by using the analysis of Steel & Elford (1986), and treats both the meteoroid collisional lifetime (T_{coll}) and the size–frequency distribution (SFD) of meteoroids ejected from the source body as free parameters. On the one hand, the collisional lifetime T_{coll} describes the variation of the spatial density of meteoroids with heliocentric distance and ecliptic latitude, and this parameter has been modeled by Pokorný et al. (2018, 2019) using the method proposed by Steel & Elford (1986). However, given that the initial estimate of T_{coll} in the inner solar system produces low values that are not consistent with the orbital elements observed by radars, Pokorný et al. (2014) inferred an average scaling factor (F_{coll}) of 20 to match the observations with modeling results. That is, the corrected collisional lifetime,¹² $T_{\text{coll}}^{\text{corr}}$, is $T_{\text{coll}}^{\text{corr}} = F_{\text{coll}} \times T_{\text{coll}}$. On the other hand, the SFD essentially characterizes the contribution of each particle size to the overall mass input of a given meteoroid population, and ultimately it depends on the dynamical evolution of meteoroids produced by radiative forces. Accordingly, the SFD characterizes the overall number of particles, $n(D)$, for a given size bin within the diameter range (D_1 , D_2) by using a single power law:

$$n(D) \propto \int_{D_1}^{D_2} D^{-\sigma} dD = \frac{1}{\sigma-1} [D_2^{-\sigma+1} - D_1^{-\sigma+1}] \quad (1)$$

where D is the geometric mean between the size delimiters, D_1 and D_2 , of each bin; the exponent σ is the differential size index at the source, which can be expressed in terms of the differential mass index δ through the conversion equation $\sigma = 3\delta - 2$. For simplicity, all of the results in the present study are estimated using the differential size indices discussed by Carrillo-Sánchez et al. (2020a), assuming a different parameterization for each meteoroid population at their respective sources: $\sigma = 4.6$ for JFCs, $\sigma = 4$ for ASTs, and $\sigma = 4$ for HTC. Note that the SFDs of each meteoroid population change to some extent during the dynamical evolution from their sources to sinks—sublimation, impact on a solar system body, or departure from the solar system.

Figure 2 shows the normalized radiant distribution of meteoroid impacts in Mars’ orbit estimated by the DMZC for the JFCs (left-hand panels), ASTs (middle panels), and HTCs (right-hand panels) and three orbital positions: aphelion ($L_s = 71^\circ$), perihelion ($L_s = 251^\circ$), and the first crossing of the ecliptic plane (FCEP) ($L_s = 325^\circ$); see Figure 1 for more details. The overall normalized fluxes are expressed in ecliptic coordinates, where the abscissa axis represents the ecliptic longitude, λ , corrected by the subsolar terminator ($a = \lambda - \lambda_0 = 0^\circ$ at 12 hr in Local True Solar Time, hereafter LTST), and the ordinate axis b is the latitude measured from the orbital plane of Mars (Figure A1 in Appendix A shows the corresponding normalized distributions for the OCCs). In the case of the JFCs, the radiant maps at aphelion (Figure 2(a)) and perihelion (Figure 2(b)) are concentrated at equatorial latitudes in the antihelion ($a = 180^\circ$, LTST = 0 hr, midnight side) and

helion ($a = 0^\circ$, LTST = 12 hr, noon side) directions, respectively, whereas most of the impacts come from the nightside at the FCEP (Figure 2(c)). These shifts in the radiant maps are essentially produced by perturbation of the angle formed by the orbital state vectors of Mars—the radial position vector (\mathbf{r}) in a heliocentric frame of reference and the velocity vector ($\mathbf{v} = \frac{d\mathbf{r}}{dt}$)—due to the eccentricity of its orbit (see Pokorný et al. 2018 and Janches et al. 2020 for more details). For comparison, Earth does not exhibit significant shifts in the radiant maps due to its near-circular orbit (Janches et al. 2020). In this respect, the angle between these two orbital state vectors is invariably 90° at perihelion and aphelion, resulting in a symmetric radiant distribution of the meteoroid fluxes. This means that the midnight and noon sides are exposed to equivalent fluxes in these orbital positions, but the more Mars moves away from perihelion (or aphelion), the more this symmetry is disturbed (Szalay et al. 2019). Like the JFCs, the AST meteoroids also exhibit a shift in the normalized distribution as Mars moves toward, or away, from the Sun (Figures 2(d), (e), and (f)), with the meteoroid fluxes concentrated around midnight in the FCEP. Finally, unlike the radiant maps of the JFCs and the ASTs, meteoroids released from the HTCs follow more eccentric and inclined orbits, resulting in a lesser disturbance by the pronounced eccentricity of Mars. Consequently, HTC particles are located around the apex direction ($a = 270^\circ$, LTST = 6 hr, dawn terminator) with a symmetric and broader radiant distribution with respect to the Martian equator and regardless of the orbital position (Figures 2(g), (h), and (i)), even though the DMZC further predicts for the HTCs a relatively significant contribution from toroidal sources—those located at latitudes $b \sim \pm 60^\circ$.

Apart from the meteoroid flux, the entry velocity of the body is a critical parameter for assessing its effect in the upper atmosphere of Mars. Figure 3 shows the average velocity distributions (v_{avg}) in kilometers per second for three meteoroid populations and two particle diameters, $D = 50 \mu\text{m}$ (top panels) and $D = 1000 \mu\text{m}$ (bottom panels). In contrast to the radiant distributions of the fluxes, the average velocity distribution for a given particle size does not change significantly along Mars’ orbit; therefore, these panels only show the corresponding results at perihelion. In the case of the JFCs (Figures 3(a) and (b)) and the ASTs (Figures 3(c) and (d)), both the helion and antihelion directions are populated by relatively faster particles at the equator of Mars. However, v_{avg} peaks in the apex direction ($a = 270^\circ$) for larger meteoroids from the JFCs (Figure 3(b)), while the north and south toroidal sources may also contribute to some extent for the ASTs (Figure 3(d)). Finally, the presence of both particles in retrograde orbits with relatively high inclination leads to the maximum values of v_{avg} for the HTCs in the apex direction (Figures 3(e) and (f)). Figure A2 in Appendix A shows the velocity distributions for the OCCs.

Figure 4 shows the normalized velocity distributions in Mars’ orbit for all those diameters considered by the DMZC (color-shaded profiles) for the three meteoroid populations studied in this manuscript at perihelion (see Figure A3 in Appendix A for the OCCs). The solid-black lines represent the normalized overall fluxes as a function of impact velocity. Note that both the profiles of the velocity distributions for the different particle sizes and the overall fluxes are normalized to an area equal to the unity. As expected, the JFCs (Figure 4(a)) and the ASTs (Figure 4(b)) are mostly characterized by slow

¹² According to Pokorný et al. (2020), the fudge factor, F_{coll} , might be somehow related to the structural nature of the meteoroid such as the bulk porosity or the hardness, even though actually there are no experimental measurements to confirm this hypothesis.

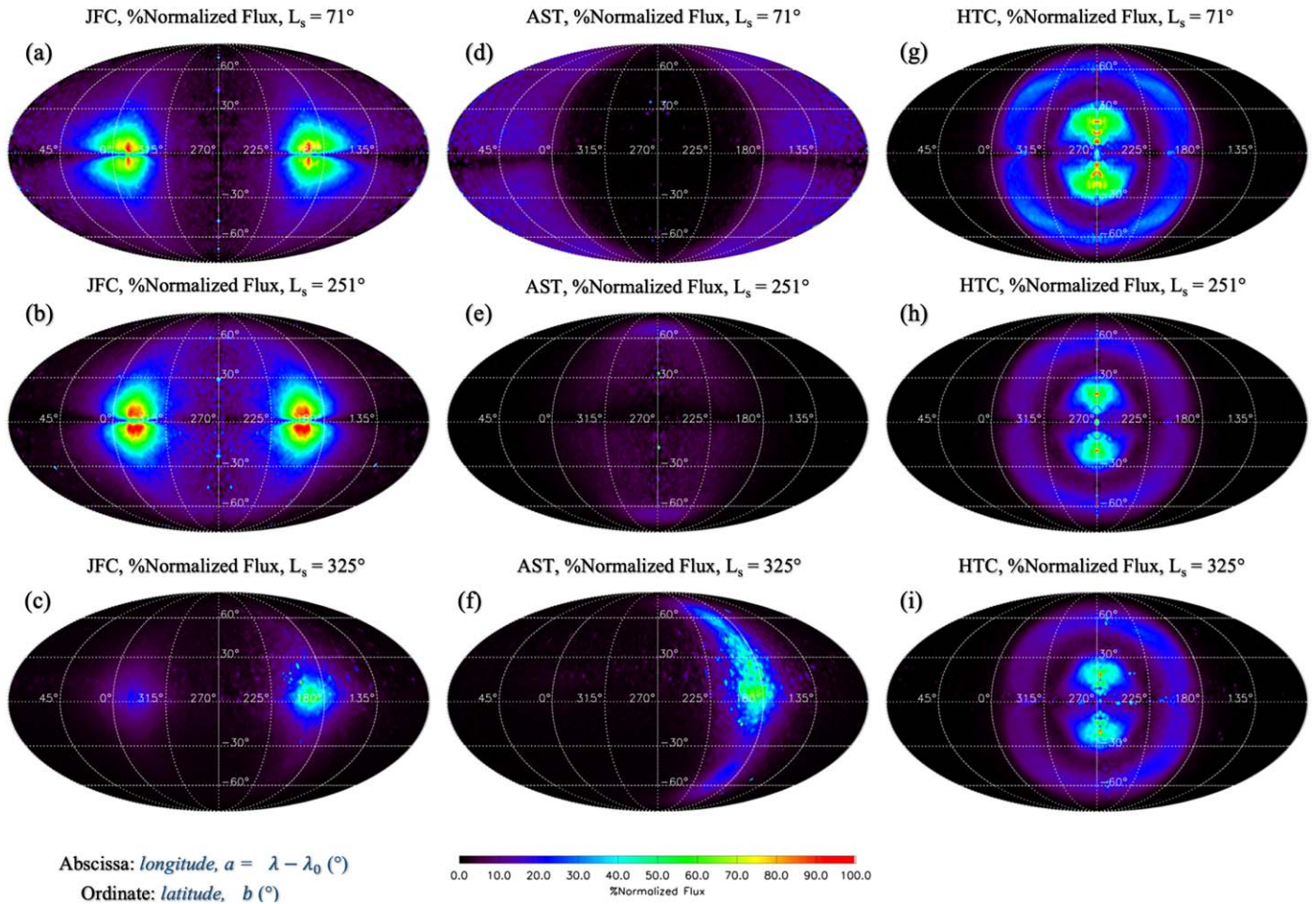


Figure 2. Normalized radiant distributions of meteoroid fluxes in Mars' orbit predicted by the DMZC for three populations: the JFCs (a, b, and c), the ASTs (d, e, and f), and the HTCs (g, h, and i), and three orbital positions: aphelion ($L_s = 71^\circ$, top panels), perihelion ($L_s = 251^\circ$, middle panels), and first crossing of the ecliptic plane ($L_s = 325^\circ$, bottom panels). The abscissa axis represents the ecliptic longitude, λ , corrected by the subsolar terminator ($a = \lambda - \lambda_0 = 0^\circ$ at 12 hr), and the ordinate axis b is the latitude measured from the orbital plane of Mars.

particles in prograde orbits peaking between $\sim 5 \text{ km s}^{-1}$, close to the escape velocity of Mars, and $\sim 10 \text{ km s}^{-1}$. As shown in Figure 3, the velocity distribution is shifted to slightly higher values with increasing particle sizes. In the case of JFCs, the dynamical evolution of small particles is practically undisturbed by collisions, in contrast to larger particles, which are significantly influenced by mutual collisions, even though only a small fraction of these larger bodies in retrograde orbits are perturbed by the gravitational pull of Jupiter (Pokorný et al. 2018). Therefore, these larger and faster bodies are mainly concentrated around the apex (Figure 3(b)). For the ASTs, small particles exhibit low eccentricities and, consequently, they may easily pass through the mean motion resonances with Jupiter, whereas larger bodies may be trapped in these mean motion resonances where either their eccentricities are altered and increased, or they may be destroyed by mutual collisions. In the case of the HTCs (Figure 4(c)), the velocity distribution for diameters $D \leq 400 \mu\text{m}$ follows a bimodal trend with a dominant peak around 25 km s^{-1} , which corresponds to particles in prograde orbits, and a secondary maximum at 50 km s^{-1} for particles in retrograde orbits. For diameters $D > 400 \mu\text{m}$, the dominant peak is shifted to around 30 km s^{-1} , whereas the retrograde component is clearly flattened because larger particles in retrograde orbits are strongly

influenced by both mutual collisions and planetary scattering in Jupiter- and Saturn-crossing orbits.

Carrillo-Sánchez et al. (2020a, 2020b, 2016) sampled the global velocity distributions (solid-black lines in Figure 4) using a Monte Carlo selection to generate a pseudo-distribution of the velocity, which was then extended to all of the representative particle sizes in the ZCM. In the present work, we will assume the corresponding velocity distribution for each single particle size (color-shaded profiles in Figure 4) rather than an overall distribution. Consequently, the contribution of larger particles to the global ablation rate will be better constrained, especially for the long-period comets.

2.2. The Meteoroid Input Function at Mars

As mentioned in Section 2.1, the DMZC provides high-resolution maps of the mass flux of meteoroids and the impact velocities as a function of the ecliptic longitude and the latitude measured from the orbital plane of Mars. The radiant distributions in ecliptic coordinates then need to be transformed into equivalent planetographic coordinates to assess the impact of meteoroid fluxes on a given planetary body. In fact, Carrillo-Sánchez et al. (2020a) assumed a constant radiant distribution of meteoroids throughout orbital position. Subsequently, the ecliptic coordinates were transformed into representative local

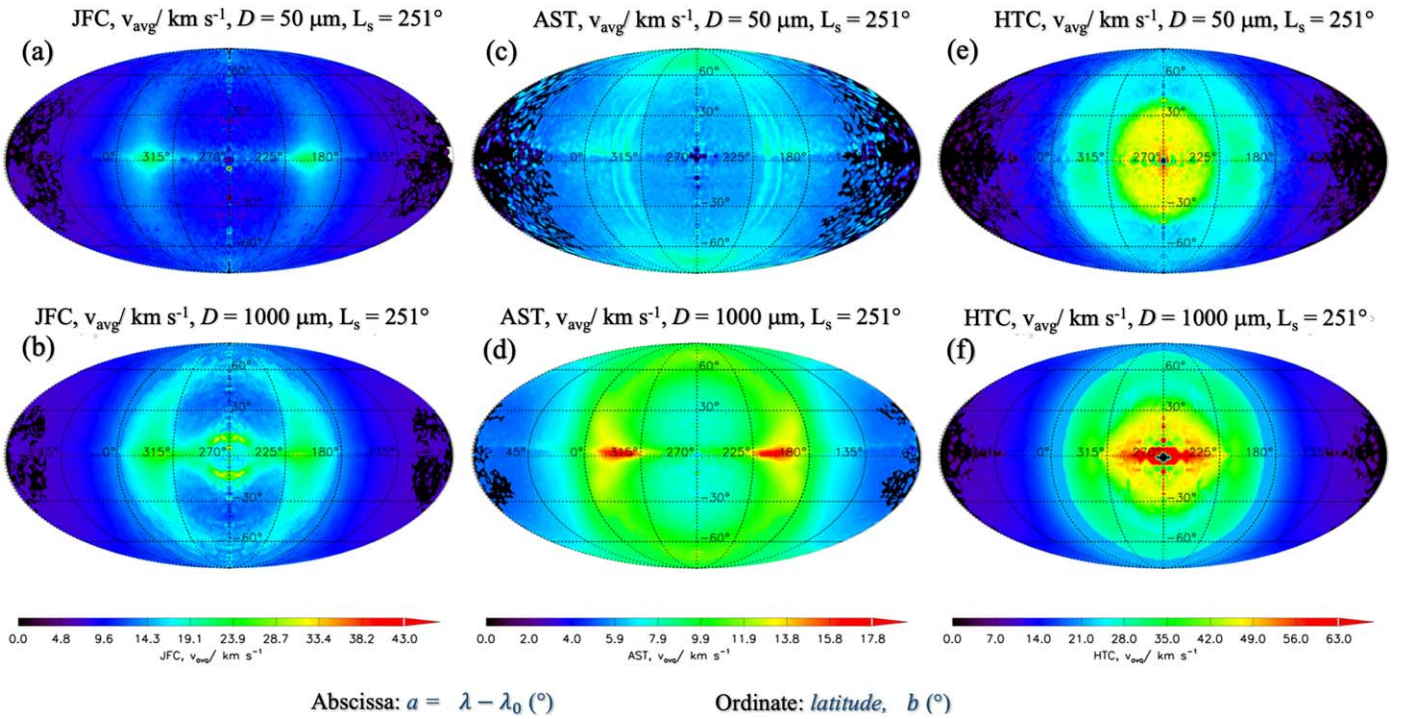


Figure 3. Average velocity distributions (in kilometers per second) of meteoroids in Mars' orbit predicted by the DMZC from the JFCs (a and b), the ASTs (c and d), and the HTC (e and f), and two particle diameters: $D = 50 \mu\text{m}$ (top panels) and $D = 1000 \mu\text{m}$ (bottom panels). The abscissa axis represents the ecliptic longitude, λ , corrected by the subsolar terminator ($a = \lambda - \lambda_0 = 0^\circ$ at 12 hr), and the ordinate axis b is the latitude measured from the orbital plane of Mars. In the case of the JFCs and HTCs, the average velocity distribution for a given particle size does not change significantly with the orbital position and, therefore, these panels only show the corresponding results at perihelion ($L_s = 251^\circ$). Note that the color scales are different for each meteoroid population.

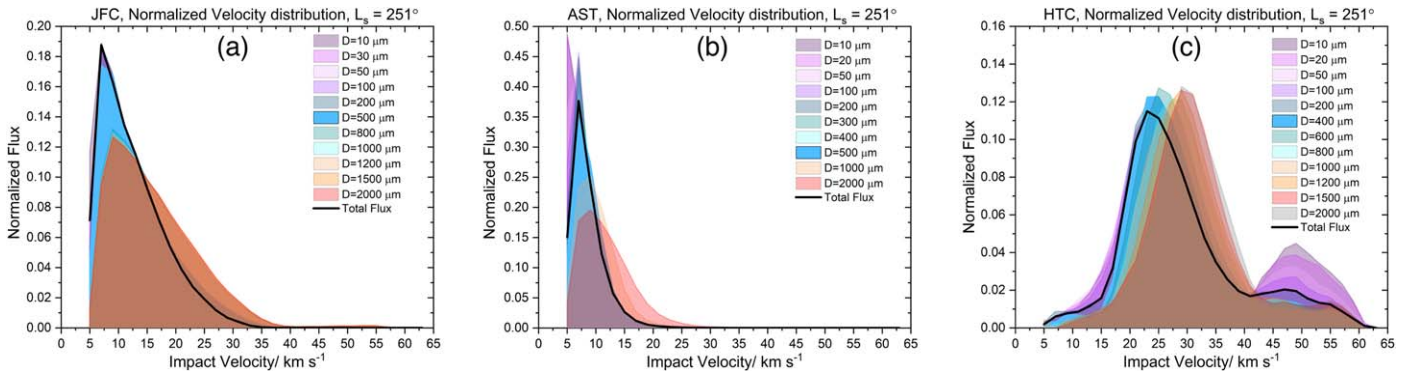


Figure 4. Normalized velocity distributions in Mars' orbit for the JFCs (a), the ASTs (b), and the HTCs (c) at perihelion ($L_s = 251^\circ$). The color profiles show the results for all of those diameters modeled by the DMZC. The solid-black line also represents the normalized overall flux for each meteoroid population as a function of the impact velocity. Note that both the profiles of the velocity distributions for the different particle sizes and the overall flux are normalized to an area equal to the unity.

coordinates at 40°N , removing any temporal, latitudinal, and seasonal variability. Aiming to address this modeling limitation, Janches et al. (2020) developed a comprehensive model able to characterize spatially and temporally the size and velocity distributions of the most relevant meteoroid populations for the inner solar system's bodies. In this manner, the MIF model determines that the density of particles crossing a planet's orbit over an entire year in a size bin D , with impact velocity v , and a radiant in ecliptic coordinates (a, b), can be expressed as:

$$N(D, v, a, b) = \omega(D, v, a, b) \cdot n(D) \quad (2)$$

where $n(D)$ is the number of particles described by the differential size index σ (see Equation (1)), and $\omega(D, v, a, b)$ is the weighting factor estimated by the DMZC.

The overall mass influx in a local cell of a planetographic grid for given mass bin m (or diameter D) with a velocity v and during a time interval Δt , is estimated as:

$$\psi_{\text{cell}}(D, v, \theta) = N(D, v, a, b) \cdot \sin(\theta(\Delta t, \Gamma, \phi)) \cdot m \cdot A_{\text{cell}}(\Gamma, \phi) \quad (3)$$

where Γ and ϕ are the planetographic latitude and longitude; and $\theta(\Delta t, \Gamma, \phi)$ is the elevation angle of the impinging meteoroid measured from the local horizon for an observer placed on a cell with planetographic coordinates Γ and ϕ during a time interval Δt , calculated from the corresponding radiant distributions provided by the DMZC and using the SPICE Toolkit (Acton 1996; Janches et al. 2020). $A_{\text{cell}}(\Gamma, \phi)$ is

the area of a cell in the planetographic grid, expressed as:

$$A_{\text{cell}}(\Gamma, \phi) = \int_{\Gamma_1}^{\Gamma_2} \int_{\phi_1}^{\phi_2} r^2 \cos \phi d\phi d\Gamma$$

$$= r^2 \Delta\Gamma [\sin \phi_2 - \sin \phi_1] \quad (4)$$

where $A_{\text{cell}}(\Gamma, \phi)$ is the area of a cell centered at (Γ, ϕ) in the planetographic grid with a fixed size bin $\Delta\Gamma = \Delta\phi = 5^\circ$, and r is the volumetric mean radius of Mars (3389.5 km). In the present study, we compute the relationship between the planetographic longitude Γ and the LTST for a given Julian Date using the method described in the Mars-LMD model (Millour & Forget 2008). Janches et al. (2020) approximated the LTST from Γ for each orbital position assuming that the maximum mass influx of the OCCs invariably occurs at LTST = 6 hr, that is, at the apex direction. However, the numerical procedure included in the present study can capture slight fluctuations in the position of the maximum flux of the OCC particles close to the apex due to the excursion of Mars from the ecliptic plane.

The following is a summary of the diurnal distributions of the average sizes and velocities estimated by the MIF model and, in all cases, the axial tilt—or obliquity—of Mars ($\varepsilon = 25.19^\circ$) leads to a latitudinal northward/southward motion. Figure 5 shows the diurnal variability of the average diameter distribution, D_{avg} , in microns for the main meteoroid populations impacting on Mars' atmosphere as a function of LTST and the latitude, for three orbital positions. D_{avg} is estimated by the MIF model from the centroid of the size distribution for each planetographic cell with coordinates (LTST, ϕ). For comparison: (1) JFCs (Figures 5(a), (b), and (c)) are the main contributor of small particle sizes with D_{avg} ranging from 51.9–56.8 μm , and the largest sizes impacting at perihelion around 18 hr in northern mid-latitudes ($10^\circ < \phi < 30^\circ$, Figure 5(b)); (2) in contrast, the AST population (Figures 5(d), (e), and (f)) provides a broader range for D_{avg} from 390.1–597.2 μm , with the largest sizes impacting at perihelion (Figure 5(e)) and the FCEP (Figure 5(f)), and mainly concentrated at $-10^\circ < \phi < 40^\circ$ after the noon (LTST > 12 hr); and (3) in the case of the HTC, D_{avg} ranges between 278.2 and 341.0 μm with a constant dawn/dusk asymmetry regardless of the orbital position. Figure 5 shows that both the JFCs and the ASTs exhibit similar characteristics due to analogous distributions of the orbital elements: (1) the larger sizes exhibit a minimum at aphelion (Figures 5(a) and (d)); and (2) there is a shift in the diurnal size distribution as Mars moves from aphelion to the FCEP as a result of the pronounced eccentricity ($e = 0.0934$) and inclination ($i = 1.85^\circ$) of Mars' orbit. In contrast to the JFCs and ASTs, the HTCs (and OCCs, see Figure A4 in Appendix A) follow a different pattern with smaller D_{avg} concentrated at the apex direction/dawn terminator (LTST = 6 hr), and larger D_{avg} around the antiapex/dusk terminator (LTST = 18 hr).

Figure 6 shows the diurnal and latitudinal variability of the average velocity, v_{avg} , in kilometers per second for three meteoroid populations arriving at the Martian atmosphere. In the case of the JFCs, v_{avg} ranges from 7.8–12.9 km s^{-1} , with faster bodies concentrated between the midnight side and noon, whereas the slower bodies are centered around the antiapex direction (18 hr). The ASTs and HTCs exhibit opposite extremes in terms of v_{avg} : while the ASTs (Figures 6(d), (e), and (f)) are principally populated by the slowest bodies with v_{avg} between 5.5 (escape velocity of Mars) and 7.2 km s^{-1} , the HTCs (Figures 6(g), (h), and (i)) provide the faster and broader distribution of v_{avg} from

11.1–35.3 km s^{-1} along with constant dawn/dusk asymmetry, and the fastest particles in retrograde orbits located at the apex direction/dawn terminator (6 hr). Note that v_{avg} from the JFCs, ASTs, and HTCs is to some extent modulated by the orbital velocity of Mars ($v_{\text{orb}} = 21.2 \text{ km s}^{-1}$ at aphelion and $v_{\text{orb}} = 26.5 \text{ km s}^{-1}$ at perihelion) and, therefore, while the minimum v_{avg} appears at aphelion (Figures 6(a), (d), and (g)), perihelion is characterized by particles with relatively faster v_{avg} (Figures 6(b), (e), and (h)). Furthermore, there is a shift in the latitudinal evolution of the velocity distributions of the JFCs and the HTCs as Mars moves from aphelion to the FCEP, due to the nonzero eccentricity and orbital inclination. However, v_{avg} from the ASTs manifests both a latitudinal and a temporal shift along Mars' orbit and, in this case, the shift pattern of v_{avg} in ASTs is comparable to the shift of its diurnal size distribution (Figures 5(d), (e), and (f)).

2.3. Modeling the Latitudinal and Seasonal Variation of Meteoric Ablated Metals at Mars with the Chemical Ablation Model

As mentioned above, the main goal of the present study is to provide for the first time a complete description of the temporal, vertical, latitudinal, and seasonal fluctuations of the deposition rates of the main meteoric metals in the upper atmosphere of Mars. For this purpose, we will use the most recent version of the CABMOD model (Carrillo-Sánchez et al. 2020b) developed at the University of Leeds to quantify the ablation rate profiles of 10 chemical species—Si, Mg, Fe, Al, Ca, Ti, P, Na, K, and Ni—of an impacting meteoroid given its initial mass, velocity, and entry angle. CABMOD includes a multiphase treatment to account for the ablation rates from both the silicate bulk (Vondrak et al. 2008) and the Fe–Ni metal domains present in IDPs (Bones et al. 2019; Carrillo-Sánchez et al. 2020a), assuming that these two phases are completely immiscible in the molten particle due to density differences (Hutchinson 2004; Gómez-Martín et al. 2017). Therefore, CABMOD uses two independent thermodynamic modules to compute the vapor pressures of metals, which are called separately when the corresponding melting temperature of each phase is reached: $\sim 1760 \text{ K}$ for the Fe–Ni metal grains (Swartzendruber et al. 1991) and $\sim 1800 \text{ K}$ for an olivine phase with a chondritic Fe: Mg ratio of 0.84 (Vondrak et al. 2008). The thermodynamic modules in the CABMOD model are: (1) the MAGMA thermodynamic module (Fegley & Cameron 1987; Schaefer & Fegley 2004) for the olivine phase, which has been recently updated with a regular solution (Banya 1993) to describe the speciation of meteoric P in PO and mainly PO₂ in the upper atmosphere (Carrillo-Sánchez et al. 2020b); and (2) the FeNi thermodynamic module to estimate the vapor pressures for pure metallic Fe and Ni (Bones et al. 2019; Carrillo-Sánchez et al. 2020a) from the JANAF thermodynamic tables (Chase et al. 1985), corrected by the corresponding Raoultian activity coefficients (Conard et al. 1978). Additionally, in this study we make three assumptions about the physical properties of the particle: (1) the elemental abundances in the meteor¹³ are defined by a CI chondritic composition (see Table A1 in Appendix A; Lodders & Fegley 2011); (2) the mass of the particle is calculated

¹³ According to the International Astronomical Union, a meteor is the light and associated physical phenomena (heat, shock, and ionization) that result from the high-speed entry of either a meteoroid or an asteroid into a gaseous atmosphere. In the present study, we will use the term meteor in the description of the thermal ablation process and, therefore, in both the CABMOD and CABMOD-MIF models.

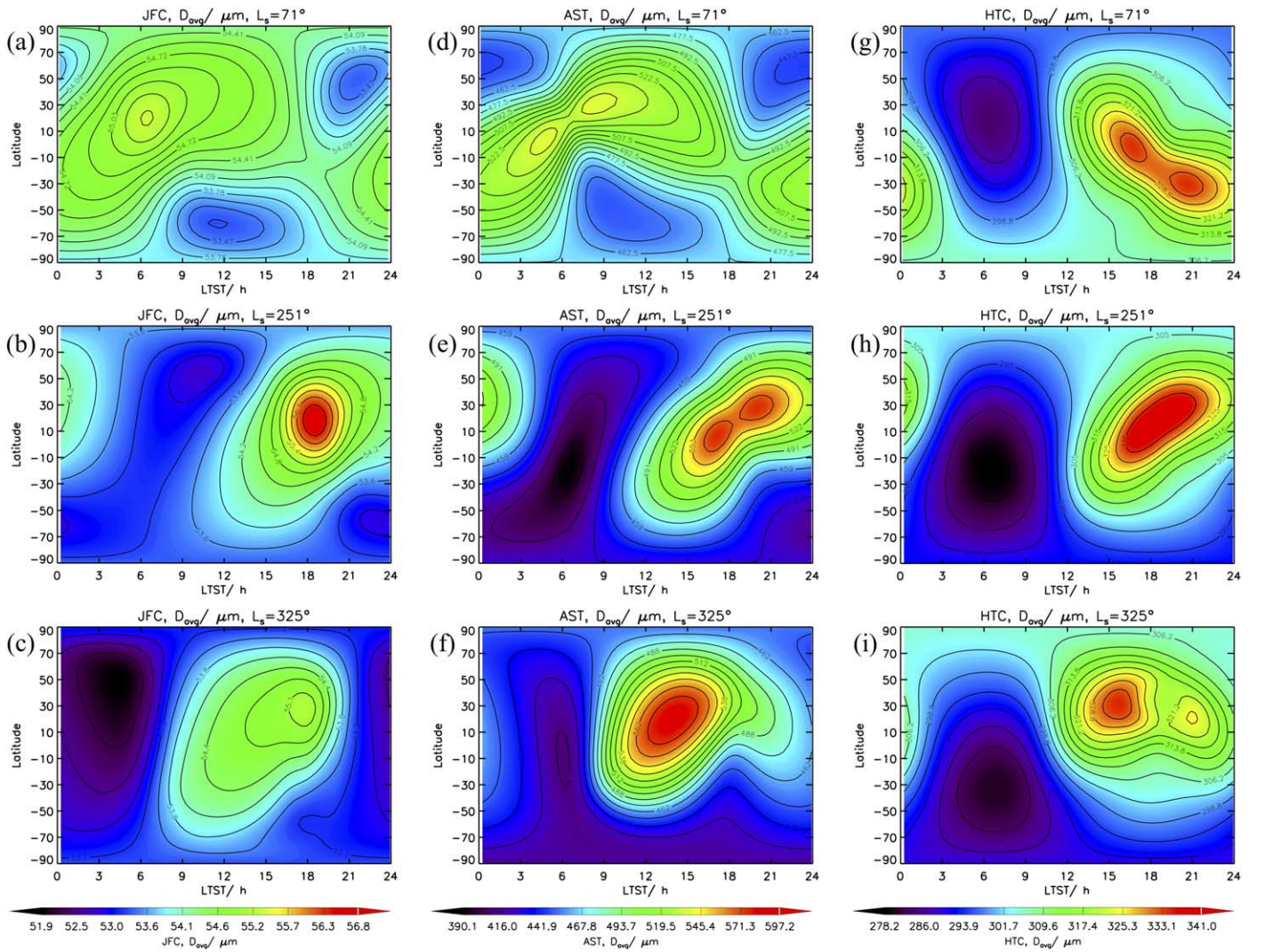


Figure 5. Diurnal variability of the average diameter distribution (in microns) of meteoroids into the Martian atmosphere determined by the MIF model for the JFCs (a, b, and c), the ASTs (d, e, and f), and the HTCs (g, h, and i) and three orbital positions: aphelion ($L_s = 71^\circ$, top panels), perihelion ($L_s = 251^\circ$, middle panels), and first crossing of the ecliptic plane ($L_s = 325^\circ$, bottom panels). These distributions are represented as a function of the Local True Solar Time and the latitude on Mars. Note that the color scales are different for each meteoroid population.

assuming a spherical shape with a silicate bulk density for CI chondrites of 1570 kg m^{-3} (Flynn et al. 2018); and (3) only particles with $D \leq 1500 \mu\text{m}$ are sampled in the CABMOD-MIF model to ensure that the meteoroids heat isothermally, which is a fundamental assumption in the model (Vondrak et al. 2008).

As discussed in detail in Section 1, Carrillo-Sánchez et al. (2020a) estimated the deposition rates of metals for the local conditions of the Martian winter at 40°N assuming that the meteoroid mass, velocity, and radiant distributions were constant both latitudinally and seasonally. Therefore, it is necessary to develop a new model to fully describe the temporal, vertical, latitudinal, and orbital variability of the injection rates of meteoric metals. The CABMOD-MIF model combines both the MIF model (Janches et al. 2020) that provides a complete description of the initial sizes, impact velocities, and entry angles of the meteoroids for 346 orbital positions with a fixed planetographic bin $\Delta\Gamma = \Delta\phi = 5^\circ$, and the CABMOD model's simulations (Carrillo-Sánchez et al. 2020b) for the atmospheric density profiles of 11 latitudes ($\phi = -90^\circ, -80^\circ, -60^\circ, -40^\circ, -20^\circ, 0^\circ, 20^\circ, 40^\circ, 60^\circ, 80^\circ,$

and 90°) and four orbital positions ($L_s = 0^\circ, 90^\circ, 180^\circ,$ and 270°) using the MCD database.

In essence, changes in atmospheric density profiles give rise to shifts of the altitude of the metal ablation peaks and to a lesser extent the overall mass ablated fraction of a meteor into the upper atmosphere. Figure 7 depicts the shift of the altitude of the ablation peak of Na in kilometers predicted by the CABMOD model as a function of the initial diameter of the particle and the impact velocity for a fixed zenith angle of 45° —the zenith angle is defined as $ZA = 90^\circ - \theta(\Delta t, \Gamma, \phi)$. Note that to assess changes of the ablation peak altitude, we only considered those particles exceeding a temperature of 1800 K in order to ensure complete melting of both silicate bulk and Fe-Ni metal grains, thereby ensuring the onset of the thermal ablation process. For example, in the case of a particle with $D = 200 \mu\text{m}$ and $v = 20 \text{ km s}^{-1}$, the ablation peak of Na is 64 km (Figure 7(a)) for a latitude $\phi = -90^\circ$ and $L_s = 90^\circ$ (northern summer/southern winter), whereas Na peaks around 30 km higher for $\phi = 60^\circ$ and $L_s = 270^\circ$ (northern winter/southern winter), a striking demonstration of the marked

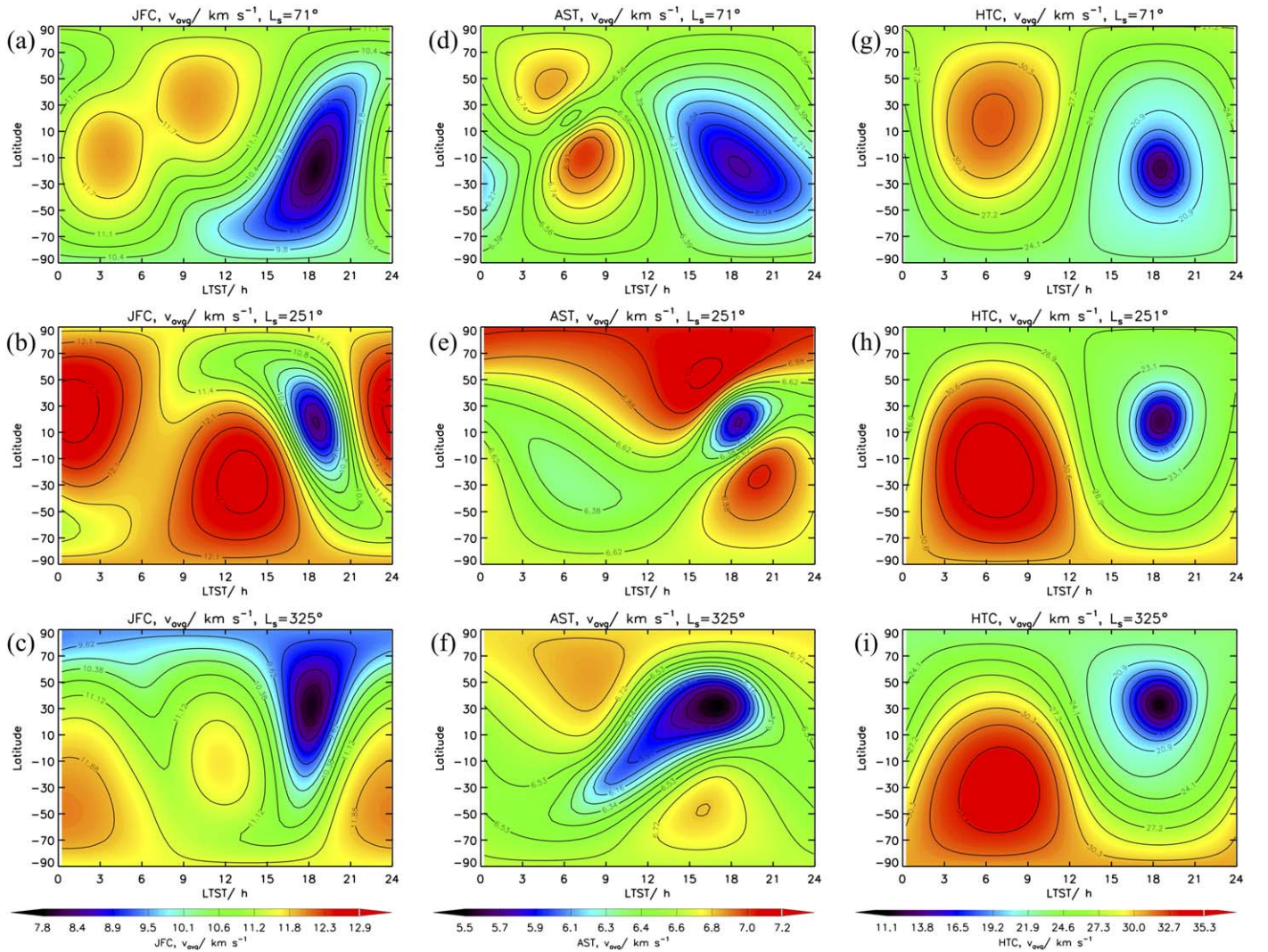


Figure 6. Diurnal variability of the average velocity distribution (in kilometers per second) of meteoroids into the Martian atmosphere determined by the MIF model for the JFCs (a, b, and c), the ASTs (d, e, and f), and the HTCs (g, h, and i) and three orbital positions: aphelion ($L_s = 71^\circ$, top panels), perihelion ($L_s = 251^\circ$, middle panels), and first crossing of the ecliptic plane ($L_s = 325^\circ$, bottom panels). These distributions are represented as a function of the Local True Solar Time and the latitude on Mars. Note that the color scales are different for each meteoroid population.

dependence that the ablation peaks of meteoric chemical species have on the vertical profiles of the atmospheric density. In this respect, the atmospheric density and temperature profiles are closely linked and, therefore, a cooling of the aerobraking region—between the mesosphere and lower thermosphere—shifts to lower altitudes the minimum atmospheric density level necessary to start thermal ablation (see Figure A6 in Appendix A). In this way, the atmospheric warming in $L_s = 270^\circ$ at a latitude $\phi = 60^\circ$ leads to higher ablation altitudes (Figure 7(b)), whereas particles ablate at lower altitudes in southern winter ($L_s = 90^\circ$) at $\phi = -90^\circ$ (Figure 7(a)). Interestingly, the overall ablation efficiency of a meteor is also affected by the atmospheric density structure. For example, the mass ablated fraction of a particle with $D = 200 \mu\text{m}$ and $v = 20 \text{ km s}^{-1}$ is 80% at $L_s = 90^\circ$ and $\phi = -90^\circ$ (Figure 8(a)) and 60% at $L_s = 270^\circ$ and $\phi = 60^\circ$ (Figure 8(b)), indicating that the colder the atmospheric temperature profile is, the deeper the penetration of the particle into the atmosphere, giving rise to a broader ablation profile and a higher ablation yield.

The CABMOD-MIF model makes several assumptions on the initial input variables used to describe and simulate realistically both the orbital parameters of the meteoroid environment around Mars and the ablation conditions of the impinging particles during their atmospheric entry. Accordingly, there are mainly three sources of uncertainty in the development of the CABMOD-MIF model, which are discussed in Appendix A.1: (1) the size and velocity distributions used by the DMZC and, consequently, the MIF model; (2) the description of the initial mineralogical structure and the chemical composition of the particle bulk assumed by the CABMOD model, and the potential alteration of the physical properties of the particles during their atmospheric entry before ablating; and (3) the vertical profiles of the Martian atmospheric density provided by the MCD database used in the CABMOD model’s simulations. All of these factors ultimately characterize the main features of the ablated meteoric metals in the upper atmosphere, such as the peak ablation altitudes, the relative ablated fractions, and the broadness of the ablation profiles.

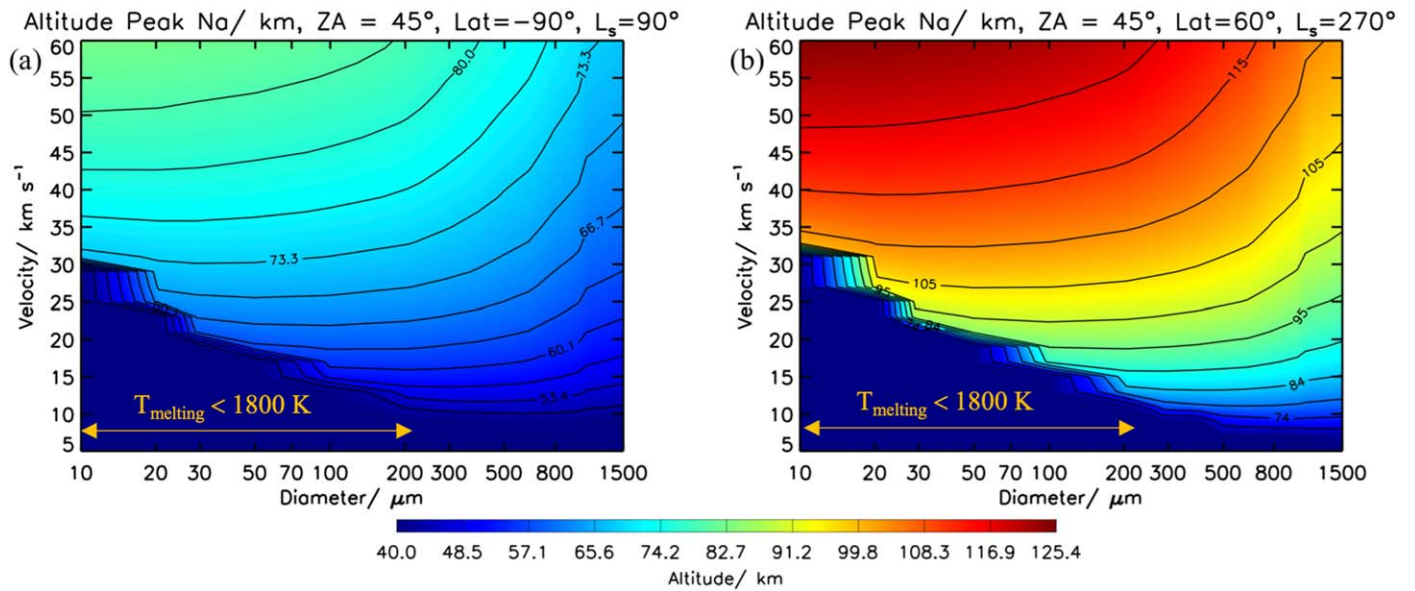


Figure 7. Altitude (in kilometers) of the ablation peak of Na predicted by the CABMOD model as a function of the initial diameter and entry velocity of the meteor, and a fixed zenith angle (ZA) of 45° . Figure 6(a) shows the altitude peaks for a latitude of -90° and a solar longitude $L_s = 90^\circ$ (northern summer/southern winter), and Figure 6(b) represents a planetographic latitude of 60° and a solar longitude $L_s = 270^\circ$ (northern winter/southern summer). The area shaded in dark blue represents all those particles that do not reach the melting temperature of 1800 K. The wavy structure of the contours is an artifact caused by the discretization of the particle size distribution.

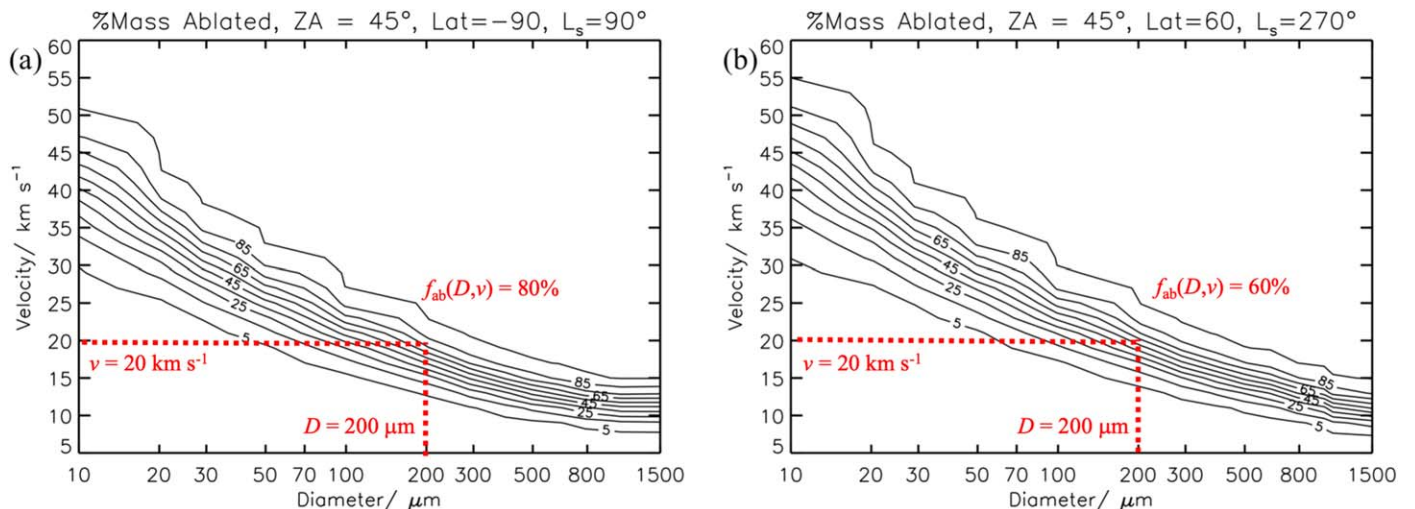


Figure 8. Mass ablated fraction of a meteor, f_{ab} , estimated by the CABMOD model as a function of initial diameter and entry velocity, and a fixed ZA of 45° . The left panel shows the ablated fraction for a Martian latitude of -90° and a solar longitude $L_s = 90^\circ$ (northern summer/southern winter), and the right panel represents a Martian latitude of 60° and a solar longitude $L_s = 270^\circ$ (northern winter/southern summer). The dashed red lines indicate the ablation fraction of a particle with an initial diameter of $200 \mu\text{m}$ entering at 20 km s^{-1} . Note that particles ablate more efficiently for the atmospheric conditions represented in panel (a): the ablation efficiencies are 80% (left panel) and 60% (right panel), respectively. The wavy structure of the contours is an artifact caused by the discretization of the particle size distribution.

3. Results and Discussion

3.1. Assessment of the Diurnal Distributions of the Meteoroid Mass Flux and the Ablation Yield of Meteoric Chemical Species

Figure 9 illustrates the diurnal variability of the relative mass influx of meteoroids estimated by the MIF model (Janches et al. 2020) for the JFCs (Figures 9(a), (b), and (c)), ASTs (Figures 9(d), (e), and (f)), and HTC (Figures 9(g), (h), and (i)), and three orbital positions: aphelion ($L_s = 71^\circ$, top panels), perihelion ($L_s = 251^\circ$, middle panels), and FCEP ($L_s = 325^\circ$, bottom panels), in the upper atmosphere of Mars as a function

of the planetographic latitude (ϕ) and LTST. The corresponding results for the OCCs are shown in Figure A7 in Appendix A. According to the DMZC simulations, the mass influx of each meteoroid population throughout Mars' orbit is essentially modulated by the combination of an eccentric orbit with a nonzero inclination relative to the ecliptic plane. In this regard, the maximum mass contribution of meteoroids from the JFCs and the ASTs occurs at the FCEP (Figures 9(c) and (f)), given that they are mainly concentrated around the ecliptic plane (Nesvorný et al. 2010, 2011) where the vertical distance with respect to the ecliptic plane is 0 au (see Figure 1). Likewise, meteoroid impacts from the HTCs increase with

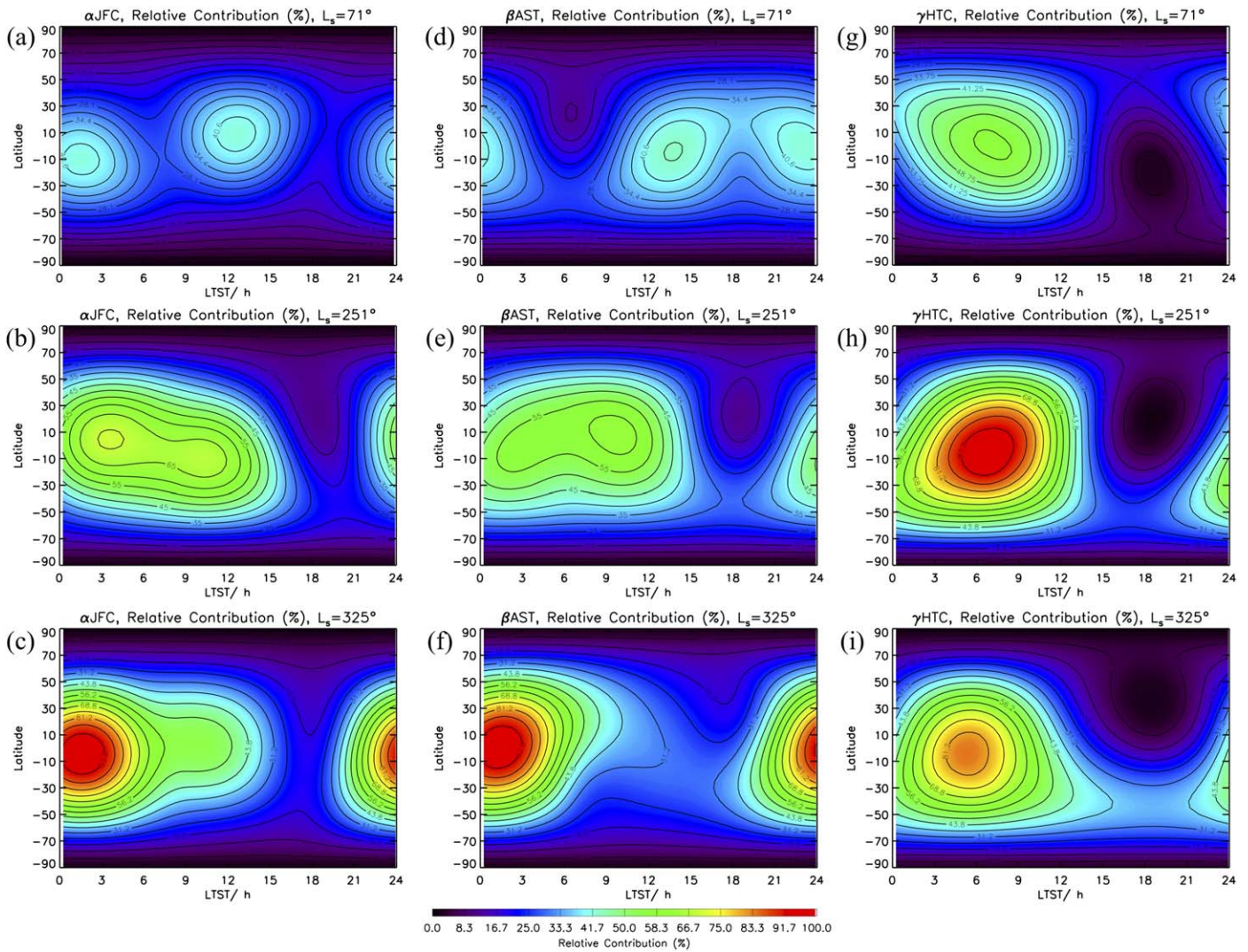


Figure 9. Diurnal variability of the relative mass influx of meteoroids into the Martian atmosphere determined by the MIF model for the JFCs (a, b, and c), the ASTs (d, e, and f), and the HTCs (g, h, and i) and three orbital positions: aphelion ($L_s = 71^\circ$, top panels), perihelion ($L_s = 251^\circ$, middle panels), and first crossing of the ecliptic plane ($L_s = 325^\circ$, bottom panels). These distributions are represented as a function of the LTST and the latitude at Mars. In all cases, the minimum mass influx occurs at aphelion. In contrast, the maximum mass input is located around the first crossing of the ecliptic plane for JFCs and ASTs, and at perihelion for HTCs.

decreasing heliocentric distance, so that the maximum contribution occurs at perihelion (Figure 9(h)). This increase of the influx is principally due to particles from the HTCs, and OCCs, which are dynamically rather different from the JFCs and the ASTs (see Section 2.1 and Pokorný et al. 2021), with typically more eccentric orbits ($e > 0.9$). As a consequence, the magnitude of the mass influx in equatorial latitudes decreases by 58%, 56%, and 43% during aphelion for the JFCs, ASTs, and HTCs (Figures 9(a), (d), and (g)), respectively.

In the same way as for the diurnal distributions of the average sizes and velocities (Figures 5 and 6), Figure 9 also shows a midnight-to-noon asymmetry of the diurnal distributions of the meteoroid impacts because of the orbital dynamics of Mars. First, meteoroids arrive preferentially from the direction of the orbital motion as Mars passes through the Zodiacal Cloud. Second, as discussed in Section 2.1, perturbations of the angle formed by the orbital state vectors of Mars, due to the eccentricity of its orbit, give rise to diurnal shifts of the meteoroid impacts. In the case of the JFCs and the ASTs, the diurnal mass fluxes at aphelion (Figures 9(a) and (d)) and perihelion (Figures 9(b) and (e)) are primarily located at around the antihelion (LTST = 0 hr) and

helion (LTST = 12 hr) directions, but most of the impacts shift to the nightside (LTST = 0 hr) as Mars moves toward the FCEP (Figures 9(c) and (f)). Unlike the JFCs and the ASTs distributions, meteoroids from the HTCs are concentrated around the dawn terminator (LTST = 6 hr) regardless of orbital position. Interestingly, the axial tilt of Mars produces an asymmetric latitudinal northward/southward motion around the midnight and noon sides for the JFC and AST populations, even though this latitudinal shift is practically negligible at the apex direction for meteoroids originating from the HTCs. In addition, in terms of the latitudinal distribution, meteoroid impacts are normally distributed around the equator, whereas the polar latitudes are barely impacted. According to the MIF model, the latitudinal dependence of impact frequencies is a consequence of two combined effects: the distribution of meteoroid sources around the ecliptic plane and the size of the surface area in the planetographic grid impacted by the particles. First, as discussed in Section 2.1, the DMZC predicts that the radiant maps of the main meteoroid sources in the sporadic background with diameters $D \leq 2000 \mu\text{m}$ are fundamentally concentrated at equatorial latitudes around the orbital plane of Mars (see Figure 2

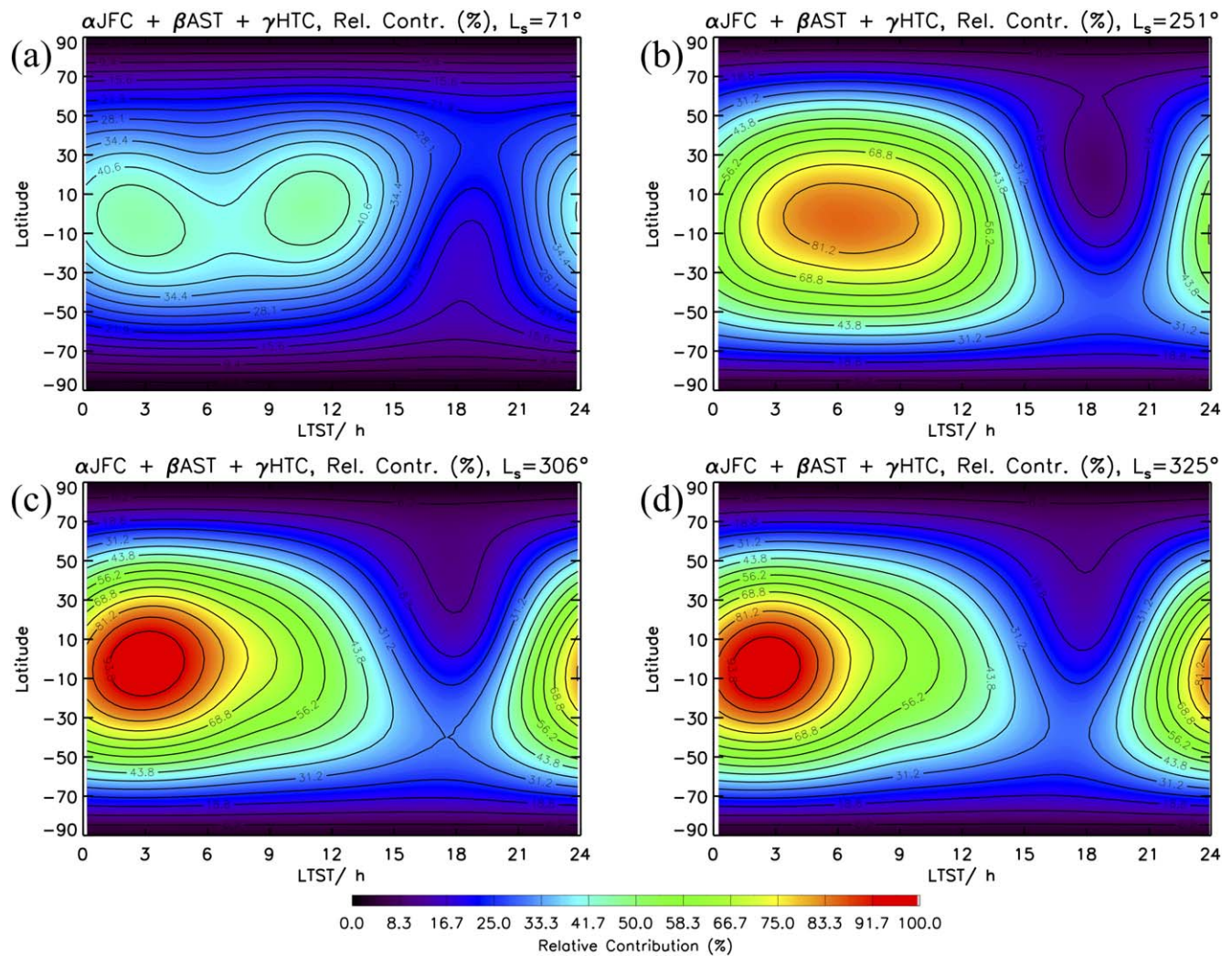


Figure 10. Diurnal variability of the relative total mass influx of meteoroids into the Martian atmosphere determined by the MIF model for four orbital positions: aphelion ($L_s = 71^\circ$, (a)), perihelion ($L_s = 251^\circ$, (b)), maximum mass input ($L_s = 306^\circ$, (c)), and first crossing of the ecliptic plane ($L_s = 325^\circ$, (d)). An animation of this figure is available, showing the variability of the total mass influx of meteoroids over a Martian year. The animation cycles through all solar longitudes, starting from $L_s = 70^\circ$, going through 0° and then to $L_s = 71^\circ$.

(An animation of this figure is available.)

as well as Figure A1 in Appendix A). Second, the surface area of the latitudinal band exposed to meteoroid impacts around Mars' equator is markedly larger than at high latitudes, resulting in a decrease of the overall meteoroid fluxes as impacts move away from the equator to the poles (Table A2 in Appendix A shows that the surface area of the equatorial band, assuming a fixed latitudinal bin of $\Delta\phi = 5^\circ$, is a factor of 23 higher than for a polar latitude $\phi = 90^\circ$). Recent studies have demonstrated a latitudinal dependence of impact frequencies: (1) preliminary calculations for the flux of extraterrestrial material falling to the Earth's surface indicate that impacts are 12% higher at the equator and 27% lower at the poles than if the flux were globally uniform (Evatt et al. 2020); and (2) unlike Evatt et al. (2020), Robertson et al. (2021) determined that the fluxes in the poles for Earth are 22% larger than the flux at the equator using the most recent models for the distributions of near-Earth objects (NEOs). Nonetheless, known NEOs are typically comets and asteroids of sizes ranging from meters to tens of kilometers, which are not circularized due to Poynting–Robertson drag, resulting in different radiant distributions to those discussed in the present work.

Carrillo-Sánchez et al. (2020a) determined the contribution of each meteoroid population at Earth's orbit, and then extrapolated the weighting factors of each population— α for JFCs, β for ASTs, and γ for HTC— for all three sources at Mars and Venus, assuming that the HTCs represent all long-period cometary particles including the OCCs. Figure 10 shows that the following features in the diurnal variability of the global fluxes at Mars' orbit following the weighting procedure discussed by Carrillo-Sánchez et al. (2020a): (1) as for the individual meteoroid populations shown in Figure 9, there is also a marked midnight-to-noon enhancement; (2) the maximum mass influx spans from $L_s = 306^\circ$ (Figure 10(c)) to the FCEP (Figure 10(d)); and (3) meteoroid impacts are fundamentally concentrated around equatorial latitudes. An animation of Figure 10 illustrating the diurnal and latitudinal variability of the total mass influx over a Martian year is available.

The ablation efficiency of a meteoric chemical compound can be defined as the ratio between the ablation rate of this compound in the upper atmosphere and the total mass input of this chemical component present in the meteoroids before ablating. Note that all of those chemical species that are not

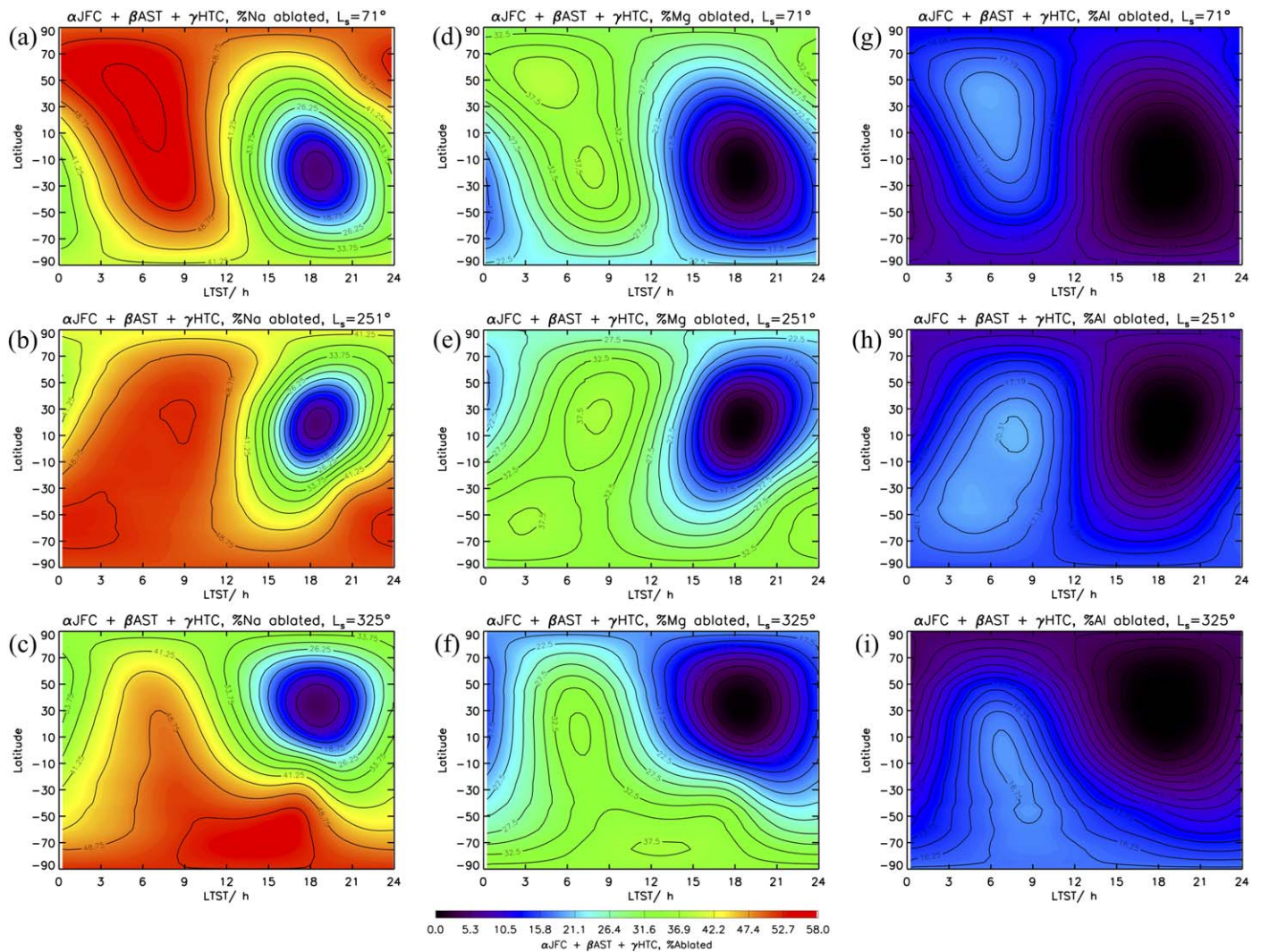


Figure 11. Diurnal variability of the fraction ablated of Na (left panels), Mg (middle panels), and Al (right panels) modeled by the CABMOD-MIF model for the JFCs (a, b, and c), the ASTs (d, e, and f), and the HTCs (g, h, and i) and three orbital positions: aphelion ($L_s = 71^\circ$, top panels), perihelion ($L_s = 251^\circ$, center panels), and first crossing of the ecliptic plane ($L_s = 325^\circ$, bottom panels).

ablated in the upper atmosphere will reach the Martian surface embedded in cosmic spherules and unmelted micrometeorites (Carrillo-Sánchez et al. 2020a). Therefore, the ablation yield assesses the combined effect of the physical properties of the particle—such as size, velocity, and entry angle distribution—and variations of the atmospheric density over the injection rates of meteoric metals, regardless of the magnitude of the total mass influx. Figure 11 shows the ablation efficiencies estimated by the CABMOD-MIF model for Na (left panels), Mg (middle panels), and Al (right panels) as a function of LTST and the latitude. First, Na exhibits higher ablation efficiencies (up to 58%), followed by Mg (up to 38%) and Al (up to 19%), largely independent of the orbital position. Second, there is a midnight-to-noon enhancement of the ablation efficiencies with a marked northward/southward motion because of the axial tilt. In this respect, the HTCs are the main contributor to the total ablated mass (see Sections 3.2 and 3.4) and, therefore, the overall ablation yields are fundamentally influenced by the size and velocity distributions of the HTCs, resulting in the highest ablation efficiencies for particles with comparatively small sizes ($D_{\text{avg}} \approx 281 \mu\text{m}$; see Figures 5(g), (h), and (i)) in retrograde orbits ($v_{\text{avg}} \approx 34 \text{ km s}^{-1}$;

see Figures 6(g), (h), and (i)). Note that the CABMOD model predicts that these small and fast particles ablate almost completely (see Figures 8(a), and (b)) and, consequently, changes of the local atmospheric conditions do not significantly perturb the ablated fraction of the meteor.

3.2. Diurnal Changes of the Deposition Rates of Ablated Metals for the Main Meteoroid Populations

The CABMOD-MIF model provides the integrated injection rate profiles of the main meteoric metals in the upper atmosphere of Mars as a function of altitude, LTST, the planetographic latitude (ϕ), and the orbital position (L_s). In this Section, we will explore the differences between the absolute injection profiles from each of the three meteoroid populations, and we will also provide overall input rate profiles for the main metals using the fitting procedure discussed in Carrillo-Sánchez et al. (2020a, 2016). Figure 12 illustrates the diurnal changes of the injection rates (in $\text{atoms m}^{-3} \text{ s}^{-1}$) of Mg estimated by the CABMOD-MIF model for the JFCs (left panels), ASTs (middle panels), and HTCs (right panels), at three orbital positions. Note that Figure 12 shows the corresponding

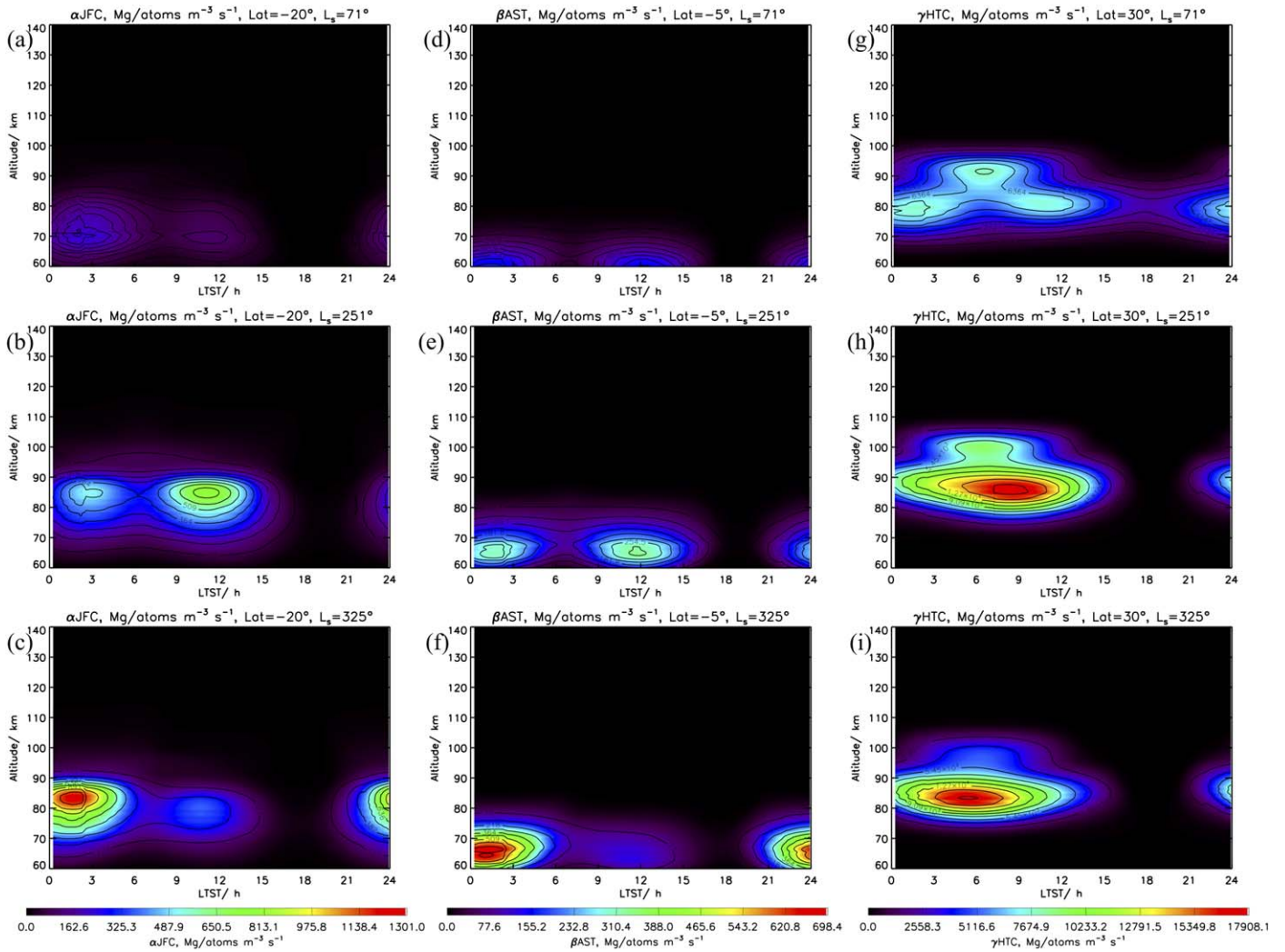


Figure 12. Diurnal variability of the injection rates (in atoms $m^{-3} s^{-1}$) of Mg estimated by the CABMOD-MIF model for the JFCs (a, b, and c), the ASTs (d, e, and f), and the HTCs (g, h, and i) and three orbital positions: aphelion ($L_s = 71^\circ$, top panels), perihelion ($L_s = 251^\circ$, middle panels), and first crossing of the ecliptic plane ($L_s = 325^\circ$, bottom panels). The corresponding latitudes of the maximum ablation rates of Mg are -20° for JFC ($L_s = 325^\circ$, (c)), -5° for the ASTs ($L_s = 325^\circ$, (f)), and 30° for the HTCs ($L_s = 251^\circ$, (h)), respectively. Note that the HTCs are comparatively the main mass contribution to the total injection rates. The color scales are different for each meteoroid population.

latitudes on Mars for the maximum ablation rates of Mg in each meteoroid population: $\phi = -20^\circ$ for JFCs, $\phi = -5^\circ$ for ASTs, and $\phi = 30^\circ$ for HTCs ($\phi = -10^\circ$ for OCCs, see Figure A8 in Appendix A). Figure 12 shows that the meteoric ablation occurs approximately between 100 and 60 km in Mars' upper atmosphere with a strong midnight-to-noon enhancement. For comparison, the HTC particles start ablating roughly 20 and 30 km higher than JFCs and ASTs, respectively, as expected from their relative velocity distributions (see Figure 6). Likewise, a simple comparison of the peak Mg ablation rates reveals that the HTC rate is a factor of ~ 14 and ~ 26 higher than for JFCs and ASTs, respectively. In terms of the temporal distribution, JFCs and ASTs exhibit two dominant lobes around the antihelion (LTST = 0 hr) and helion (LTST = 12 hr) directions; however, in the case of HTCs, there is a significant contribution to the deposition rate at the apex position (LTST = 6 hr) at relatively higher altitudes, especially at aphelion and perihelion.

The JFCs mainly contribute to small particle sizes in prograde orbits, with a narrow difference between the daily minimum and maximum values of D_{avg} and v_{avg} of 2.1–3.9 μm and 4.1–4.6 km

s^{-1} (left panels in Figures 5 and 6), respectively. As a consequence of the small size variation during a Martian day, the injection rates of JFCs are essentially modulated by the dynamical evolution of the velocity distribution and, therefore, the metal deposition at a specific latitude ($\phi = -20^\circ$ in Figures 12(a), (b), and (c)) ultimately depends on the asymmetric latitudinal northward/southward motion of the velocity distribution around the midnight and noon sides as a result of the axial tilt. In contrast, ASTs exhibit a significantly larger difference between the daily minimum and maximum values of D_{avg} with 95.8–186.6 μm (middle panels in Figure 5), along with a very narrow difference for v_{avg} of about 1 km s^{-1} (middle panels in Figure 6). Consequently, metal production from the ASTs on the midnight and noon sides at a given latitude ($\phi = -5^\circ$ in Figures 12(d), (e), and (f)) is essentially influenced by the diurnal variability of the particle size distribution. Finally, HTCs (Figures 12(g), (h), and (i)) exhibit both a broad difference of D_{avg} and v_{avg} during a Martian day (right panels in Figures 5 and 6) and, accordingly, whereas the metal deposition at the dawn terminator is populated with smaller particles in retrograde orbits, the corresponding lobes in the midnight and

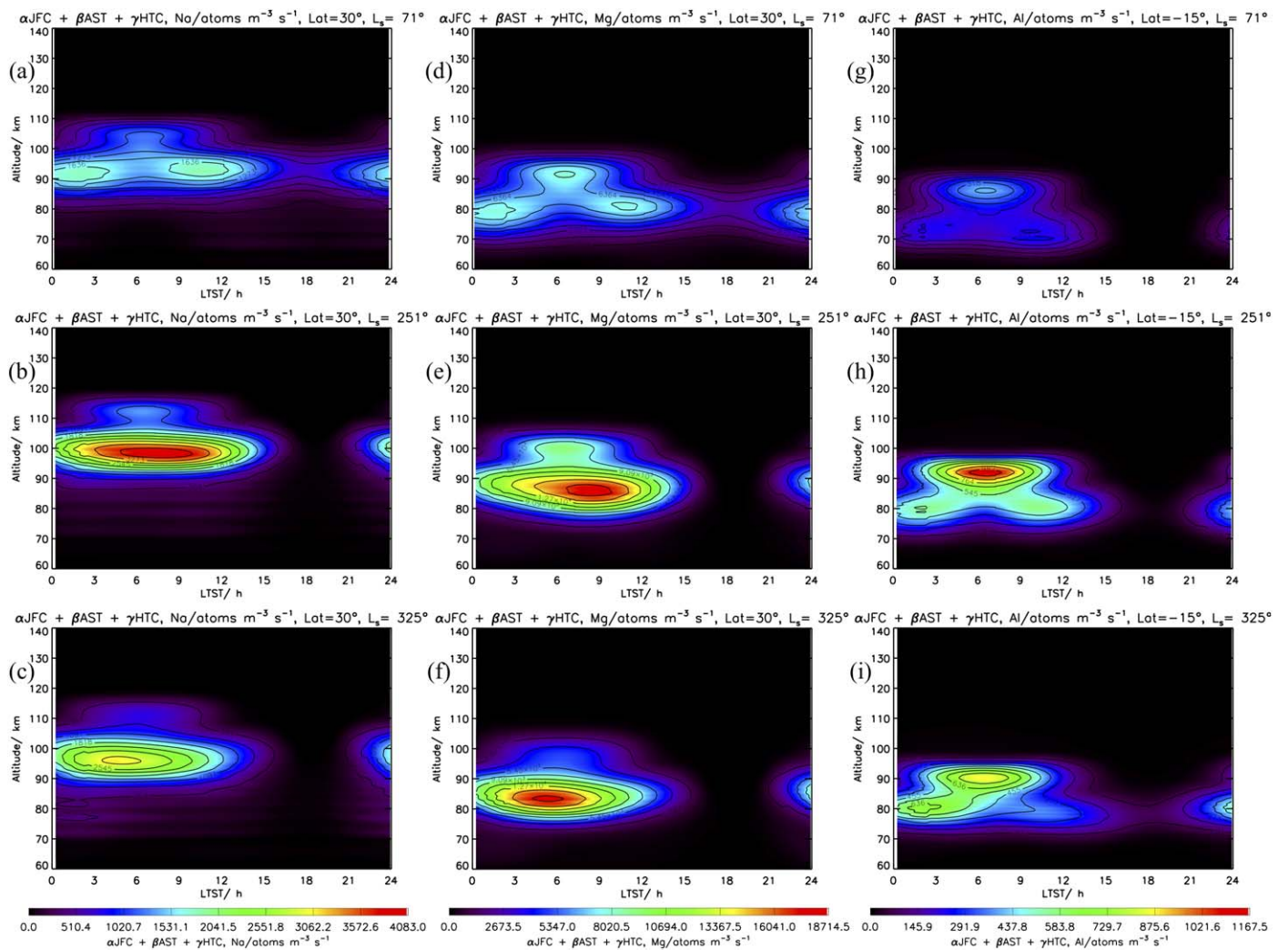


Figure 13. Diurnal variability of the total injection rates (in atoms $m^{-3} s^{-1}$) of Na (a, b, and c), Mg (d, e, and f), and Al (g, h, and i) estimated by the CABMOD-MIF model and three orbital positions: aphelion ($L_s = 71^\circ$, top panels), perihelion ($L_s = 251^\circ$, middle panels), and first crossing of the ecliptic plane ($L_s = 325^\circ$, bottom panels). The maximum ablation rates of the three metals appear at perihelion and for the Martian latitudes of 30° (Mg and Na) and -15° (Al). In the case of Al, this metal is comparatively more refractory than Na and Mg and, therefore, it is mainly injected at latitudes where small and fast particles are dominant (see Figures 4(h) and 5(h)). Note that the color scales are different for each meteoric metal.

noon sides are produced by larger particles with slower entry velocities.

Figure 13 presents the total injection rates for three meteoric metals: Na (left panels), Mg (middle panels), and Al (right panels). Note that the maximum ablation rates of these three metals appear at perihelion for the latitudes $\phi = 30^\circ$ (Mg and Na) and $\phi = -10^\circ$ (Al), respectively, since HTC are the main contributor to the total ablated input. The alkali elements (Na and K—not shown) ablate about 15 km higher than the main constituents (Mg, Fe, and Si—not shown) regardless of L_s . However, refractory elements, such as Al, are primarily released more efficiently in the dawn terminator at latitudes where small and high-momentum particles are dominant (see right panels in Figure 6). An animation of the injection rates of ablated Mg at equatorial latitudes over a Martian year is available (see also Figures 14(c), (h), (m), and (r)).

3.3. Latitudinal and Seasonal Shifts of the Peak Altitude of Ablated Metals

In this Section, we examine the combined effect of the orbital elements of Mars—that is, the axial tilt, the orbital eccentricity, and the inclination of the orbit—on the altitude

profiles of ablated metals at different latitudes and orbital positions. Figure 14 shows the average diurnal injection rates of Mg estimated by the CABMOD-MIF model at northern high latitudes ($65^\circ < \phi < 90^\circ$, panels (a), (f), (k), and (p)), northern mid-latitudes ($15^\circ < \phi < 65^\circ$, panels (b), (g), (l), and (q)), equatorial latitudes ($-15^\circ < \phi < 15^\circ$, panels (c), (h), (m), and (r)), southern mid-latitudes ($-15^\circ < \phi < -65^\circ$, panels (d), (i), (n), and (s)), and southern high latitudes ($-65^\circ < \phi < -90^\circ$, panels (e), (j), (o), and (t)). Likewise, each column in Figure 14 presents the average of the injection rates for each season: the left panels show the average rates between $L_s = 0^\circ$ (early northern spring/early southern fall) and $L_s = 90^\circ$ (early northern summer/early southern winter); panels in the second column show the average rates between $L_s = 90^\circ$ (early northern summer/early southern winter) and $L_s = 180^\circ$ (early northern fall/early southern spring); panels in the third column represent the average rates between $L_s = 180^\circ$ (early northern fall/early southern spring) and $L_s = 270^\circ$ (early northern winter/early southern summer); and the right panels show the average rates between $L_s = 270^\circ$ (early northern winter/early southern summer) and $L_s = 360^\circ$ (early northern spring/

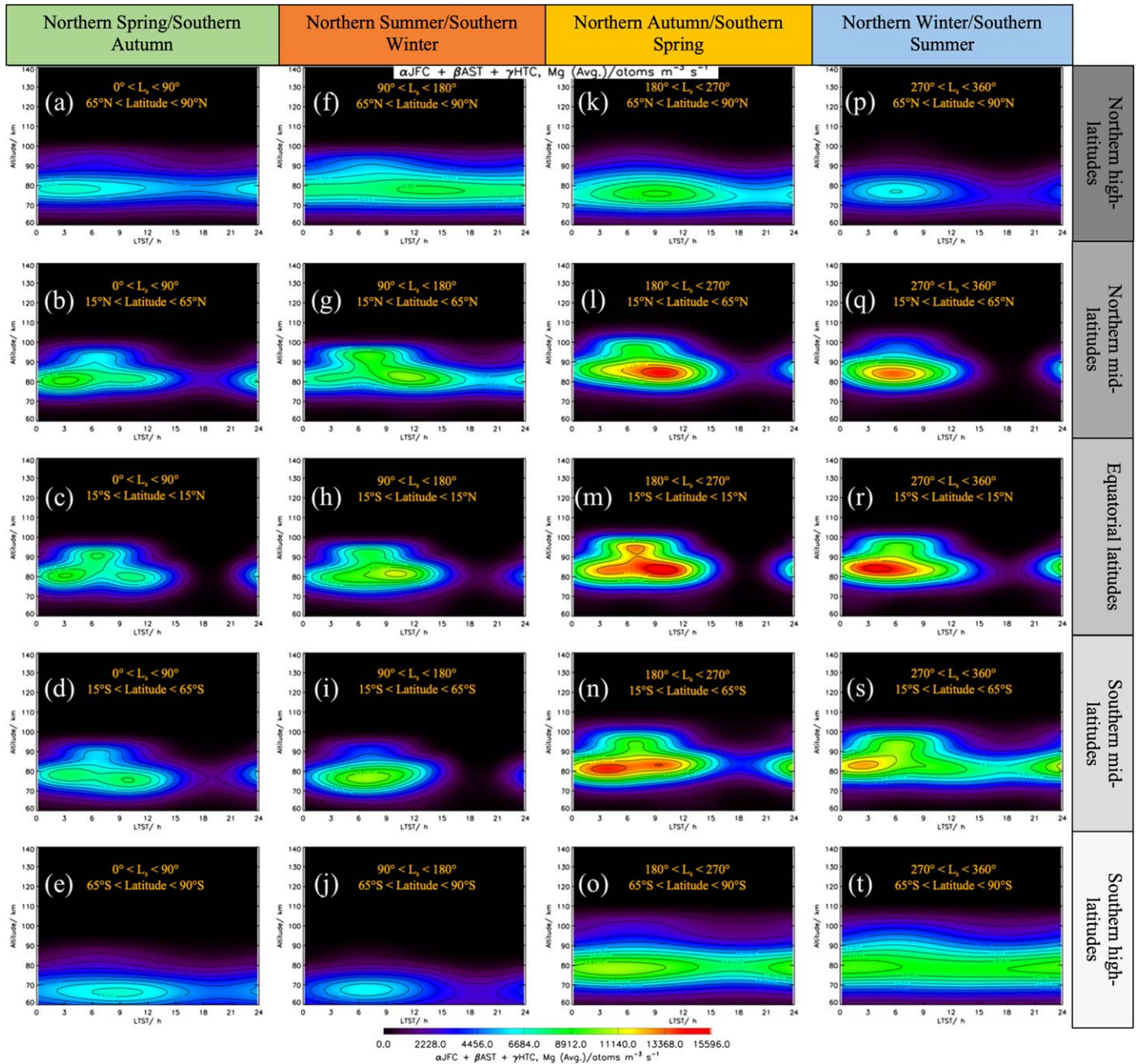


Figure 14. Average diurnal variability of the total injection rates (in atoms $m^{-3} s^{-1}$) of Mg estimated by the CABMOD-MIF model at northern high latitudes ($65^\circ < \phi < 90^\circ$, panels (a), (f), (k), and (p)), northern mid-latitudes ($15^\circ < \phi < 65^\circ$, panels (b), (g), (l), and (q)), equatorial latitudes ($-15^\circ < \phi < 15^\circ$, panels (c), (h), (m), and (r)), southern mid-latitudes ($-15^\circ < \phi < -65^\circ$, panels (d), (i), (n), and (s)), and southern high latitudes ($-65^\circ < \phi < -90^\circ$, panels (e), (j), (o), and (t)). The left panels represent the average rates between $L_s = 0^\circ$ (northern spring/southern fall) and $L_s = 90^\circ$ (northern summer/southern winter). Panels in the second column show the average rates between $L_s = 90^\circ$ (northern summer/southern winter) and $L_s = 180^\circ$ (northern fall/southern spring). The right panels show the average rates between $L_s = 180^\circ$ (northern fall/southern spring) and $L_s = 270^\circ$ (northern winter/southern summer). The right panels show the average rates between $L_s = 270^\circ$ (northern winter/southern summer) and $L_s = 360^\circ$ (northern spring/southern fall). An animation of the injection rates of ablated Mg at equatorial latitudes over a Martian year is available. The animation cycles through all solar longitudes, starting from $L_s = 70^\circ$, going through 0° and then to $L_s = 71^\circ$.

(An animation of this figure is available.)

early southern fall). For simplicity, only the corresponding results of Mg will be discussed in this Section, since all of the metals modeled by CABMOD-MIF exhibit similar latitudinal and orbital distributions.

The axial tilt is essentially responsible for the latitudinal northward/southward motion of the peak ablation altitude of meteoric chemical components. In order to exemplify the effect of axial tilt, we focus here on the seasonal conditions of

northern summer/southern winter (Figures 14(f), (g), (h), (i), and (j)). Meteoric ablation exhibits a marked midnight-to-noon enhancement at equatorial latitudes (see Figure 14(h)) with some contribution at the dawn terminator (LTST=6 hr) between 90 and 95 km, and with significantly higher injection rates around noon at 80 km. Note that the midnight-to-noon enhancement becomes attenuated at northern mid-latitudes during the summer (Figure 14(g)) and, at northern high latitudes,

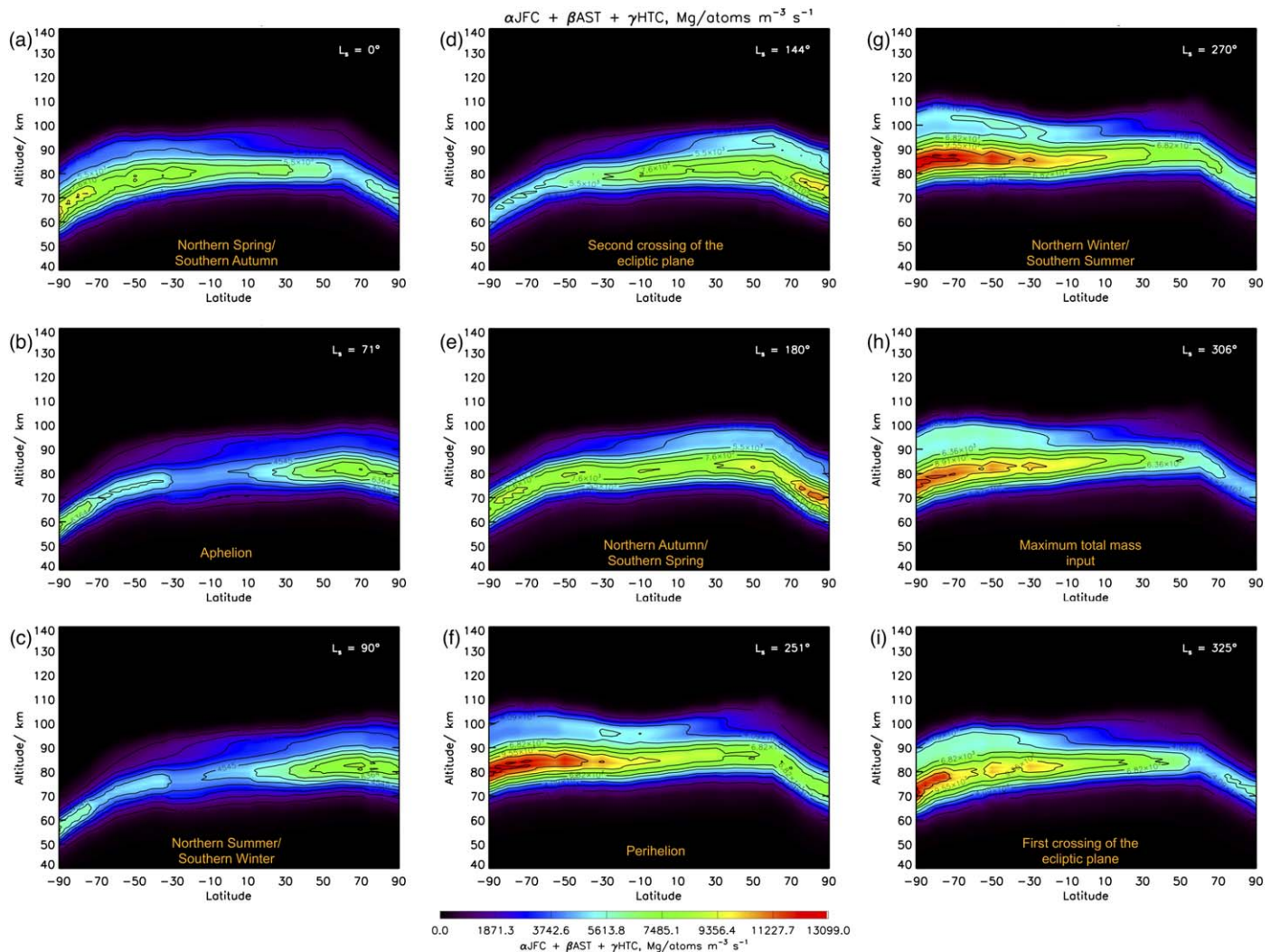


Figure 15. Seasonal variability of the total injection rates (in atoms $\text{m}^{-3} \text{s}^{-1}$) of Mg estimated by the CABMOD-MIF model and weighted over a Martian day as a function of the height (in kilometers) and the Martian latitude for the most relevant orbital positions: $L_s = 0^\circ$ (panel (a), northern spring/southern fall), $L_s = 71^\circ$ (panel (b), aphelion), $L_s = 90^\circ$ (panel (c), northern summer/southern winter), $L_s = 144^\circ$ (panel (d), second crossing of the ecliptic plane), $L_s = 180^\circ$ (panel (e), northern fall/southern spring), $L_s = 251^\circ$ (panel (f), perihelion), $L_s = 270^\circ$ (panel (g), northern winter/southern summer), $L_s = 306^\circ$ (panel (h), maximum total mass input), and $L_s = 325^\circ$ (panel (i), first crossing of the ecliptic plane). An animation of the seasonal variability of Mg as a function of the altitude and latitude is available. The animation cycles through all solar longitudes, starting from $L_s = 70^\circ$, going through 0° and then to $L_s = 71^\circ$.

(An animation of this figure is available.)

both the midnight-to-noon enhancement and the contribution from the dawn terminator disappear (Figure 14(f)). The same effects are predicted for the seasonal conditions of northern winter/southern summer (Figures 14(p), (q), (r), (s), and (t)). An animation of the injection rates of ablated Mg at equatorial latitudes over a Martian year is available.

Similarly, the eccentricity and the nonzero inclination of Mars' orbit perturb the midnight-to-noon distribution, the altitude of the ablation peak, and the magnitude of ablated atoms in a given latitude over a Martian year. On the one hand, while the deposition of Mg shifts preferentially from the midnight side and the dawn terminator (Figures 14(a), (b), and (c)) to the noon side (Figures 14(k), (l), and (m)) as Mars moves toward the northern fall from northern spring, the southern hemisphere manifests an opposite noon-to-midnight motion (Figures 14(d), (e), (n), and (o)). On the other hand, even though the maximum deposition of Mg is localized at perihelion for a latitude $\phi = 30^\circ$ (see Figure 13), the maximum average rate occurs close to the equator around the noon side as

Mars approaches the northern fall (Figure 14(m)). In the case of refractory metals, there is a marked average contribution at the dawn terminator in equatorial and mid-latitudes (see Figures A9 for Al in Appendix A).

Figure 15 presents the seasonal variability of injection rates of Mg weighted over a Martian day as a function of the height and the latitude, and the most relevant orbital positions ($L_s = 0^\circ$, $L_s = 71^\circ$, $L_s = 90^\circ$, $L_s = 144^\circ$, $L_s = 180^\circ$, $L_s = 251^\circ$, $L_s = 270^\circ$, $L_s = 306^\circ$, and $L_s = 325^\circ$). Note that the ablation rates are weighted over a latitudinal band ($0^\circ \leq \Gamma \leq 360^\circ$) centered at latitude ϕ (Table A2 in Appendix A shows the surface area of the northern latitudinal bands, $A_{\partial\phi}(\phi)$). During southern and northern fall (Figures 15(a) and (e)), the injection rates of Mg appear 20 km higher in the equatorial and mid-latitudes than in the poles, with most of the ablated Mg concentrated around the southern (Figure 15(a)) and northern (Figure 15(e)) poles, respectively. Moreover, there is a significant shift of the peak ablation height at high latitudes as Mars moves toward, or away, from northern/southern

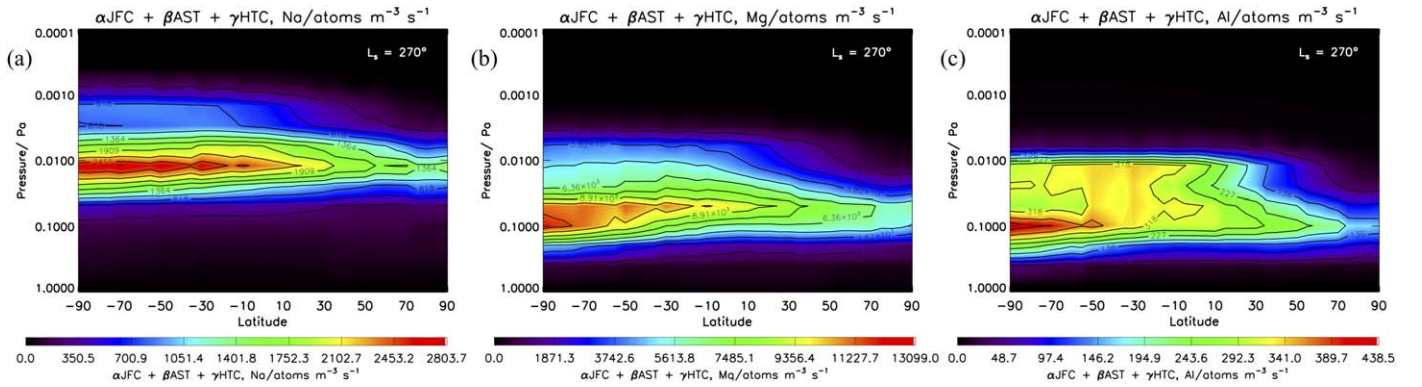


Figure 16. Seasonal variability of the total injection rates (in atoms $\text{m}^{-3} \text{s}^{-1}$) of Na (a), Mg (b), and Al (c) estimated by the CABMOD-MIF model as a function of the pressure level (in pascals) and the Martian latitude at $L_s = 270^\circ$ (northern winter/southern summer). Note that the color scales are different for each meteoric metal.

Table 1
Global Mass Input from the Three Cosmic Dust Sources for Mars at Aphelion and Perihelion

Mass Flux	JFCs (tons sol^{-1})		ASTs (tons sol^{-1})		HTCs (tons sol^{-1})		Total (tons sol^{-1})	
	Aphelion	Perihelion	Aphelion	Perihelion	Aphelion	Perihelion	Aphelion	Perihelion
Total Input Mass	0.77	1.14	0.19	0.25	0.54	0.84	1.50	2.23
Total Ablated Atoms	0.013	0.034	8.47×10^{-3}	0.015	0.39	0.67	0.41	0.72
Na	1.26×10^{-3}	2.83×10^{-3}	3.37×10^{-4}	4.99×10^{-4}	9.61×10^{-3}	0.015	0.011	0.018
K	5.28×10^{-5}	1.19×10^{-4}	3.55×10^{-5}	5.26×10^{-5}	4.19×10^{-4}	6.57×10^{-4}	5.07×10^{-4}	8.29×10^{-4}
Fe	5.56×10^{-3}	0.015	3.83×10^{-3}	6.48×10^{-3}	0.12	0.20	0.13	0.22
Ni	4.22×10^{-4}	1.09×10^{-4}	2.95×10^{-4}	4.83×10^{-4}	7.65×10^{-3}	0.012	8.37×10^{-3}	0.013
Si	1.47×10^{-3}	3.96×10^{-3}	1.03×10^{-3}	1.90×10^{-3}	0.062	0.11	0.064	0.12
Mg	1.01×10^{-3}	2.74×10^{-3}	6.18×10^{-4}	1.22×10^{-3}	0.052	0.090	0.054	0.094
P	4.84×10^{-5}	1.21×10^{-4}	3.00×10^{-5}	4.91×10^{-5}	7.01×10^{-4}	1.12×10^{-3}	7.79×10^{-4}	1.29×10^{-3}
Ca	2.90×10^{-5}	8.53×10^{-5}	7.97×10^{-6}	2.16×10^{-5}	3.01×10^{-3}	5.72×10^{-3}	3.05×10^{-3}	5.83×10^{-3}
Al	1.67×10^{-5}	5.21×10^{-5}	3.32×10^{-6}	9.91×10^{-6}	1.99×10^{-3}	3.98×10^{-3}	2.01×10^{-3}	4.04×10^{-3}
Ti	1.42×10^{-6}	4.17×10^{-6}	4.35×10^{-7}	1.12×10^{-6}	1.46×10^{-4}	2.77×10^{-4}	1.48×10^{-4}	2.82×10^{-4}
O	3.38×10^{-3}	9.04×10^{-3}	2.28×10^{-3}	4.19×10^{-3}	0.13	0.23	0.14	0.24

Note. Elemental ablation inputs are italicized. Note that the mass fluxes are expressed in tons sol^{-1} (1 solar day at Mars is equivalent to 1.0275 Earth days).

solstices (Figures 15(c) and (g)). Therefore, while the Mg ablation height is up to 20 km lower at high latitudes compared with the equator during northern/southern winter, no such shift occurs between the equator and northern/southern summer. Furthermore, there is a marked peak in the overall Mg abundance in southern mid- and high latitudes during summer near 80–90 km (Figure 15(g)). In summary, the diurnally integrated rates of Mg appear somewhat counterintuitive: while the diurnal distributions of Mg (Figures 13–14) predict maximum ablation fluxes around Mars’ equator, the diurnally integrated rates tend to be located at mid- to high latitudes. As discussed above, the midnight-to-noon asymmetry is diminished at mid-latitudes (Figures 14(g) and (s)) and disappears at high latitudes during summer (Figures 14(f) and (t)), giving rise to a constant metal deposition in these latitudes over a Martian day and, consequently, higher diurnally integrated ablation rates. An animation of Figure 15 showing the seasonal variability of Mg as a function of the altitude and latitude over a Martian year is available.

Figure 16 shows the diurnally integrated injection rates of Na, Mg, and Al estimated as a function of atmospheric pressure (in units of pascals) and latitude, for $L_s = 270^\circ$. The alkali elements exemplified by Na are injected close to a pressure level of 0.01 Pa, whereas Mg and Al are injected at a pressure level one order of magnitude higher. Note that the metals are

always deposited around their corresponding atmospheric pressure levels regardless of orbital position.

3.4. Determining the Seasonal Variation of the Total Mass Influxes and Ablation Rates

In this Section, we explore the variation of the ablation fluxes of individual metals and the total mass inputs introduced by the eccentricity of the Martian orbit and the excursion of Mars away from the ecliptic plane. Figure 1 illustrates schematically the fluctuations of the total mass influx and ablated atoms with the orbital position (L_s). The larger contribution to the total mass input ranges from northern winter ($L_s = 270^\circ$) to the FCEP ($L_s = 325^\circ$), with a maximum at $L_s = 306^\circ$ of 2.30 tons sol^{-1} (1 solar day at Mars is equivalent to 1.0275 Earth days); the difference of the mass flux from $L_s = 306^\circ$ to $L_s = 270^\circ$ or to $L_s = 325^\circ$ is $<2\%$. In contrast, the minimum total mass input occurs between the maximum vertical distance above the ecliptic plane ($L_s = 56^\circ$) and aphelion with 1.50 tons sol^{-1} , with a decrease relative to the maximum mass influx of about 35%. Similarly, as discussed above, ablated atoms mainly arise from the HTCs with maximum rates between perihelion and northern winter with 0.71 tons sol^{-1} , while the ablation influx falls around 41% at aphelion with 0.42 tons sol^{-1} . Table 1 lists the partitioning of the total ablated mass into the individual metals modeled by the

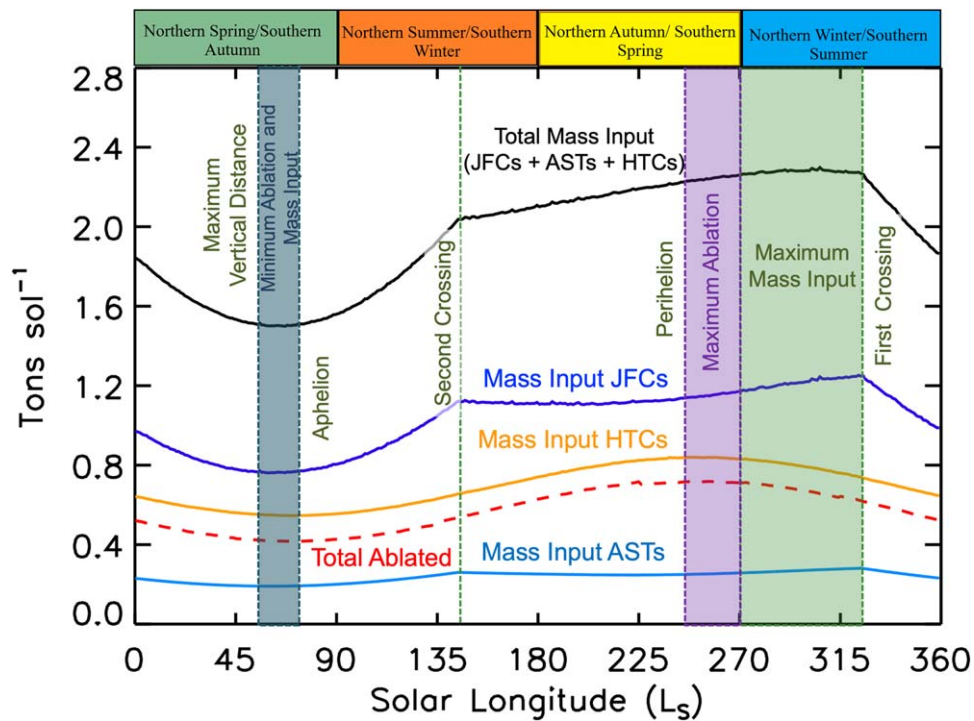


Figure 17. Seasonal variability of the mass input with the orbital position for the JFCs (dark-blue line), ASTs (light-blue line), HTCs (yellow line), total mass input (black line), and total ablated (dashed red line). Note that the mass fluxes are expressed in tons sol^{-1} (1 solar day at Mars is equivalent to 1.0275 Earth days).

CABMOD-MIF at aphelion and perihelion. Like the results reported by Carrillo-Sánchez et al. (2020a), the contribution of JFCs, ASTs, and HTCs to the overall fluxes are around 51%, 12%, and 37%, respectively, and they remain approximately constant in these two orbital positions. The global mass flux between aphelion and perihelion ranges from $1.50 \text{ tons sol}^{-1}$ to $2.23 \text{ tons sol}^{-1}$, i.e., an increase of around 50%. These estimates of the global fluxes are within the mass range of $0.088\text{--}8.84 \text{ tons sol}^{-1}$ determined by the LPW instrument on MAVEN for particles in the diameter range $2\text{--}24 \mu\text{m}$ (Andersson et al. 2015); for comparison, the CABMOD-MIF model predicts a total input of $0.11\text{--}0.16 \text{ tons sol}^{-1}$ in this size range. Additionally, the overall ablated fractions with respect to the total mass input are 27.6% and 32.0% at aphelion and perihelion, respectively, as a result of relatively faster particles at perihelion (see Section 2.2). Interestingly, the elemental ablation input increases between a factor of ~ 1.6 in the case of alkali elements—Na and K—and ~ 2 for refractory constituents—Ca, Al, and Ti.

Figure 17 shows the seasonal variability of the total mass flux of meteoroids integrated latitudinally and temporally over Mars’ surface and partitioned into JFCs (dark-blue line), ASTs (light-blue line), and HTCs (yellow line). The large contribution from the JFC source to the total accreted mass (black line) over the Martian year is consistent with observations of the Zodiacal Cloud (Zook 2001; Nesvorný et al. 2010; Rowan-Robinson & May 2013; Yang & Ishiguro 2015), even though most of these particles survive as unmelted micrometeorites (Carrillo-Sánchez et al. 2020a). The input rates of JFCs and ASTs exhibit a larger increase from aphelion to the second crossing of the ecliptic plane (SCEP, $L_s = 144^\circ$), because these meteor populations are primarily located at the ecliptic plane. Consequently, the maximum influxes of the JFCs and the ASTs occur at the FCEP, with increases of 63% and 46% compared with their corresponding minimum inputs, respectively, followed by a dramatic decrease when Mars moves

away from the FCEP. As discussed above, the HTCs are the major contributor to the ablated mass (dashed red line) with a relative increase from aphelion (minimum) to perihelion (maximum) of 54%.

Figures 18 and 19 show the integrated diurnal fluxes of the total inputs and the ablated mass for the three meteoroid populations as a function of Martian latitude and L_s . In the case of the JFCs (Figure 18(a)) and the ASTs (Figure 18(b)), their relative contributions to the total input mass account for up to 56% and 12%, respectively, between the SCEP and the FCEP around Mars’ equator ($-30^\circ < \phi < 30^\circ$). Conversely, the HTCs exhibit a pronounced latitudinal variability as a function of L_s (Figure 18(c)), caused by the obliquity of Mars and, accordingly, the relative contribution to the total input peaks around perihelion at $-40^\circ < \phi < -10^\circ$. In all cases, the combined effect of a nonzero inclination and an eccentric orbit leads to a decrease of the input magnitude around aphelion. The global mass influx after combining the three meteor populations decreases by 50% at the equator during aphelion (Figure 18(d)), and less than 20% at polar latitudes. As discussed in Section 3.1, several recent studies have demonstrated a latitudinal dependence of the impact frequencies. Finally, the total ablation rate (Figure 19(d)) follows a similar latitudinal and orbital variability as the HTCs, with a negligible contribution from particles originating from the ASTs.

4. Conclusions and Future Work

In this study we present the most complete description to date of the temporal, latitudinal, and seasonal fluctuations of the deposition rates of the main meteoric metals in the upper atmosphere of Mars. In this respect, we have combined two models: (1) the MIF (Janiches et al. 2020), which uses the DMZC model to characterize spatially and temporally the size and velocity distributions of the most relevant meteoroid

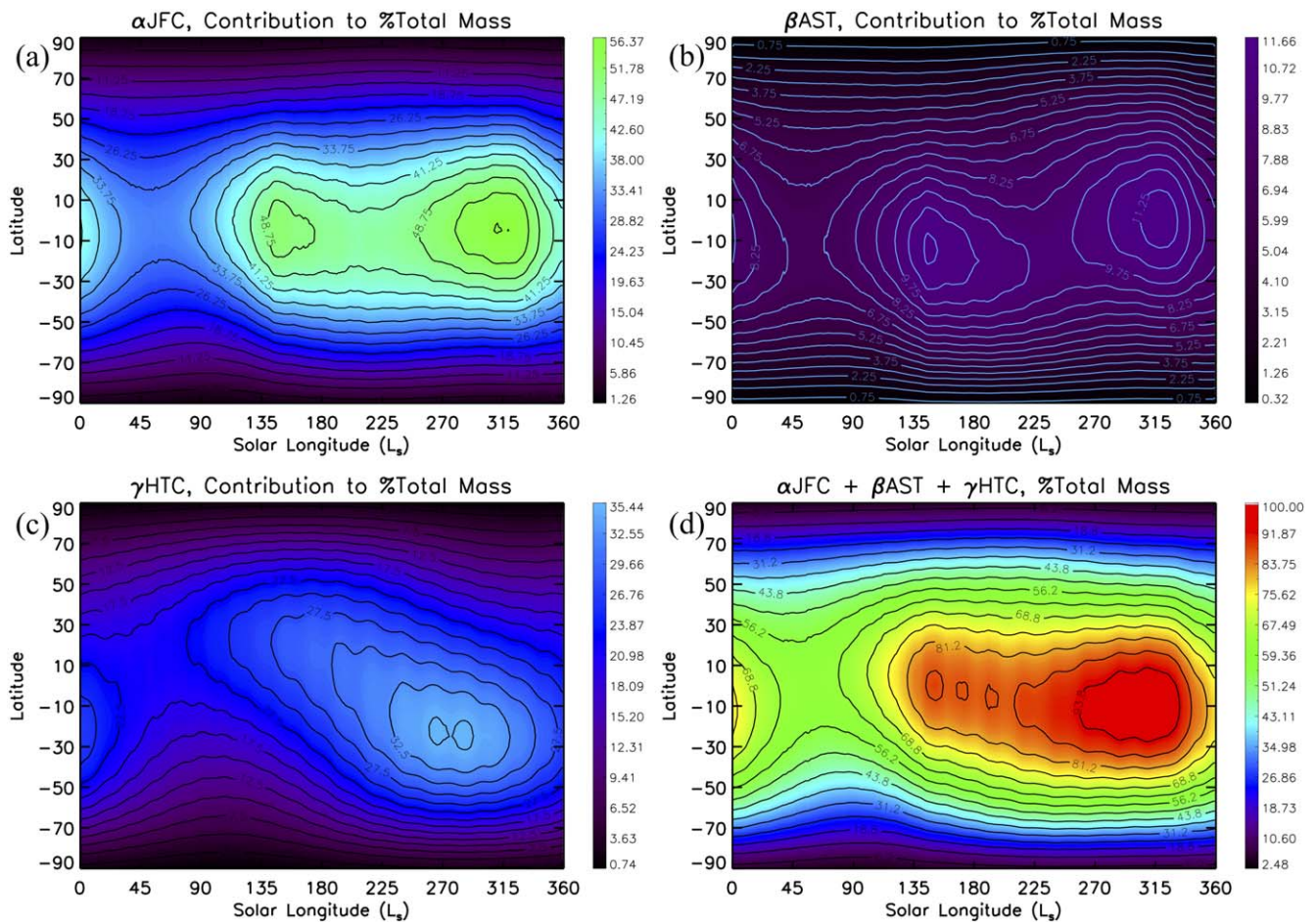


Figure 18. Seasonal variability of the contribution to the total mass influx determined by the CABMOD-MIF model for the JFCs (a), the ASTs (b), and the HTCs (c) as a function of the planetographic latitude and the solar longitude. Panel (d) represents the seasonal variability of the total mass influx.

populations in the inner solar system—JFCs, ASTs, and HTCs; and (2) the most recent version of the University of Leeds CABMOD (Carrillo-Sánchez et al. 2020b) to quantify the ablation rate profiles of 10 chemical species—Si, Mg, Fe, Al, Ca, Ti, P, Na, K, and Ni—of an impacting meteor given its initial mass, velocity, and entry angle. In summary, the modeling results indicate that:

1. Meteoroid impact flux is mostly distributed at low latitudes around the equator, whereas the polar latitudes experience relatively lower contributions.
2. The maximum total mass influx appears between the northern winter and the first crossing of the ecliptic plane, peaking at $L_s = 306^\circ$ with $2.30 \text{ tons sol}^{-1}$. The minimum mass influx occurs around aphelion with $1.50 \text{ tons sol}^{-1}$.
3. Most of the ablated atoms arise from the HTCs with a maximum input of $0.71 \text{ tons sol}^{-1}$ between perihelion and the northern winter. The minimum of the total ablated mass appears between the maximum vertical distance above the ecliptic plane and aphelion with $0.42 \text{ tons sol}^{-1}$.
4. Meteoric ablation exhibits a marked midnight-to-noon enhancement at equatorial latitudes, although this enhancement becomes attenuated at the mid- and high latitudes.
5. There is a significant shift of the peak ablation altitude at high latitudes as Mars moves toward, or away, from the northern/southern solstices.

Given the lack of direct measurements of radiant and velocity distributions of meteoroids around Mars' orbit, it is not possible to validate directly the CABMOD-MIF results with observations. However, seven Earth years of MAVEN/IUVS observations of the sporadic background of Mg^+ at Mars are available (Crismani et al. 2017; Plane et al. 2018c; Crismani et al. 2018), and these can be used to constrain the CABMOD-MIF results indirectly. In essence, the abundance of the metal ion layers is subject to both complex dynamical evolution of ablated meteoric metals and subsequent global transport dynamics and chemistry (both ion-molecule and neutral) in the upper atmosphere. Therefore, in order to explain MAVEN/IUVS observations of Mg^+ , the global injection rates of meteoric metals predicted by the CABMOD-MIF model are being implemented within a global circulation model of Mars.

Finally, we will extend this study to the atmospheres of Earth and Venus. For this purpose, the contribution of four meteor populations, including OCCs, will be reassessed assuming more recent measurements of the meteor size distribution index σ based on radar observations (Janches et al. 2019), and recent estimates of the annual accretion rates of both spherules and unmelted micrometeorites at the CONCORDIA Station located at Dome C (Antarctica; Rojas et al. 2021) in a diameter range from $12\text{--}700 \mu\text{m}$. In terms of the peak altitude of ablated metals, it is expected that the corresponding CABMOD-MIF model for Earth does not exhibit seasonal differences as marked as for Mars. Compared with Earth, these differences are basically produced for

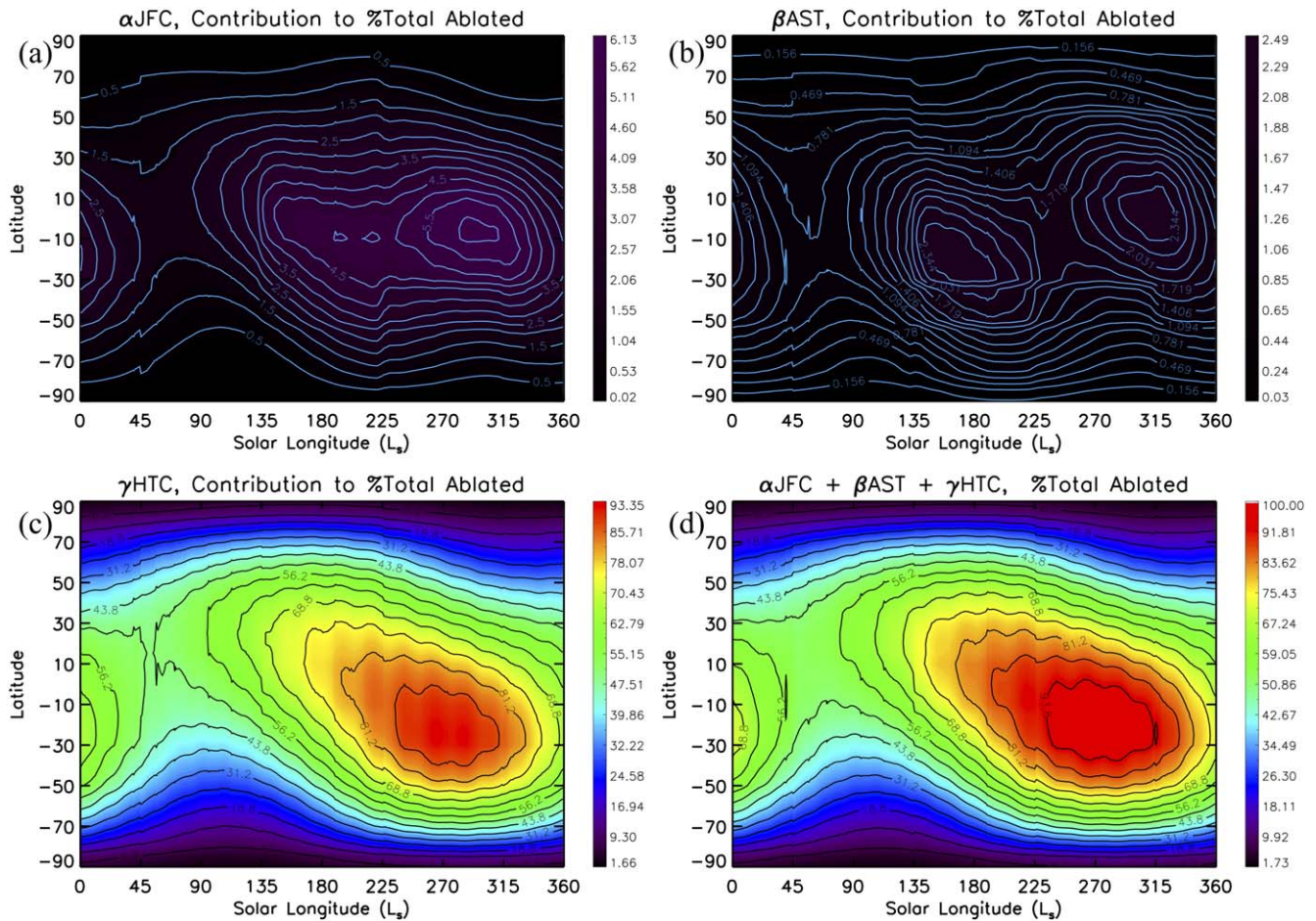


Figure 19. Seasonal variability of the contribution to the total ablated mass determined by the CABMOD-MIF model for the JFCs (a), the ASTs (b), and the HTC (c) as a function of the planetographic latitude and the solar longitude (L_s). Panel (d) represents the seasonal variability of the total mass influx.

two reasons at Mars: (1) the atmospheric densities at Mars show considerable seasonal fluctuations because of the dust content, which controls the atmospheric temperature (Forget et al. 2009); and (2) the eccentricity and the inclination of Mars— $e = 0.0934$ and $i = 1.85^\circ$ —are markedly higher than at Earth— $e = 0.017$ and $i = 0^\circ$.

This work is supported by the NASA ISFM EIMM Program and the PHaSER cooperative agreement with the Catholic University of America (grant No. 80NSSC21M0180). J.M.C. P., W.F., and D.R.M. are supported by the UK Science and Technology Facilities Council (Project ST/T000279/1). P.P. acknowledges funding from the NASA ISFM EIMM award, the NASA Cooperative Agreement 80GSFC21M0002, as supported by NASA Solar System Workings award No. 80NSSC21K0153. M.M.J.C. is supported in part by NASA award 80NSSC21M0110 through the NASA Goddard Space Flight Center. M.S. is supported by the NASA ISFM EIMM Program. D.R.M. is also supported by the National Science Foundation (grant No. 1650918). The CABMOD-MIF output are archived at the Leeds University PETAL (Petabyte Environment Tape Archive and Library; <http://www.sec.leeds.ac.uk/business-and-consultation/facilities/petabyte-environmental-tapearchiveand-library-petal/>) and are available upon request to J.D.C.S. and D.J. The CABMOD model has been optimized using the GNU Parallel shell tool (<https://zenodo.org/record/1146014#.YilLW1zMJpY>).

Declaration of Competing Interest

The authors declare that they have no known competing financial interest or personal relationships that could have appeared to influence the work reported in this paper.

Credit of Authorship

Juan Diego Carrillo Sánchez: Formal analysis, Methodology, Software, Data curation, Writing—original draft, Writing—review & editing. Diego Janches: Funding acquisition, Conceptualization, Methodology, Software, Writing—review & editing. John M. C. Plane: Methodology, Writing—review & editing. Petr Pokorný: Methodology, Writing—review & editing. Menelaos Sarantos: Methodology, Writing—review & editing. Matteo M. J. Crismani: Methodology, Writing—review & editing. Wuhu Feng: Methodology, Writing—review & editing. Daniel R. Marsh: Methodology, Writing—review & editing.

Appendix A

In this section, we summarize both the main results for the OCCs and the sources of uncertainty in the development of the CABMOD-MIF model for Mars. Figure A1 shows the normalized radiant distributions for the OCCs estimated by the DMZC and three orbital positions: aphelion A1(a), perihelion A1(b), and the FCEP A1(c). Figure A2 represents the average velocity distribution for the OCCs and two particle diameters at perihelion: $D = 50 \mu\text{m}$ (panel (a)) and $D = 1200 \mu\text{m}$ (panel (b)). As shown

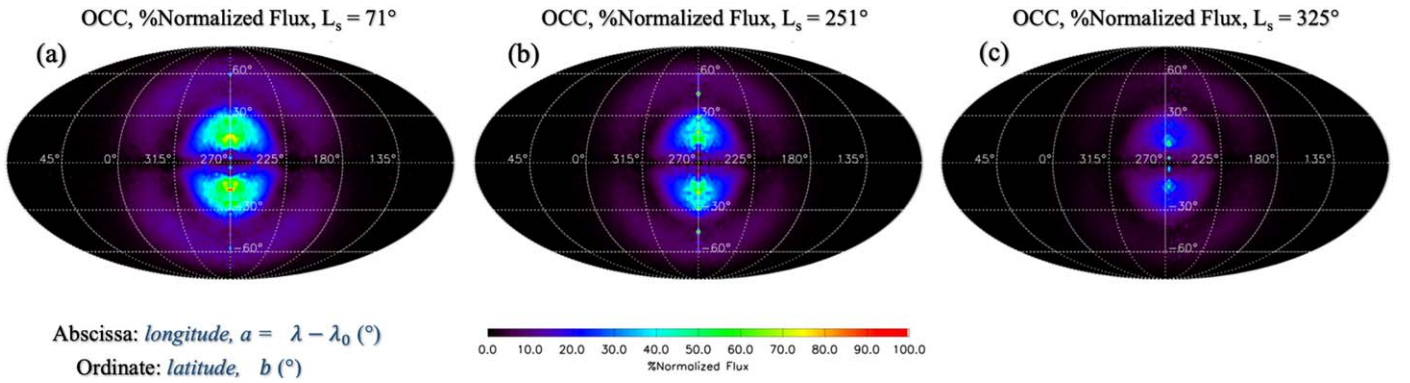


Figure A1. Normalized radiant distributions of meteoroid fluxes in Mars' orbit predicted by the DMZC for the OCCs and three orbital positions: aphelion ($L_s = 71^\circ$, (a)), perihelion ($L_s = 251^\circ$, (b)), and first crossing of the ecliptic plane ($L_s = 325^\circ$, (c)). The abscissa axis represents the ecliptic longitude, λ , corrected by the subsolar terminator ($a = \lambda - \lambda_0 = 0^\circ$ at 12 hr), and the ordinate axis b is the latitude measured from the orbital plane of Mars.

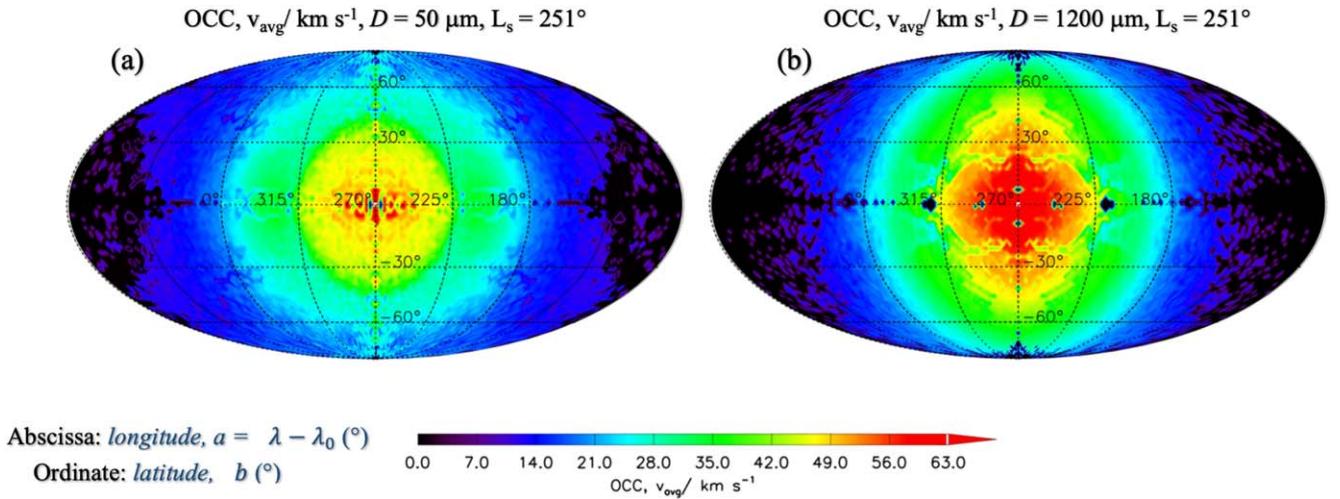


Figure A2. Average velocity distributions (in kilometers per second) of meteoroids in Mars' orbit predicted by the DMZC from the OCCs and two particle diameters: $D = 50 \mu\text{m}$ (a) and $D = 1200 \mu\text{m}$ (b). The abscissa axis represents the ecliptic longitude, λ , corrected by the subsolar terminator ($a = \lambda - \lambda_0 = 0^\circ$ at 12 hr), and the ordinate axis b is the latitude measured from the orbital plane of Mars. The average velocity distribution for a given particle size does not change significantly with the orbital position and, therefore, these panels only show the corresponding results at perihelion ($L_s = 251^\circ$).

in Figure A3, the normalized velocity distribution of the OCCs follows a bimodal trend with a dominant peak around 50 km s^{-1} which correspond to particles in retrograde orbits, and a secondary peak around 25 km s^{-1} for particles in prograde orbits. Figures A4 and A5 show the temporal and latitudinal variability of the average diameter distribution, D_{avg} , in μm and the average velocity, v_{avg} , in km s^{-1} for the OCCs and three orbital positions. Figure A6 presents the relationship between the temperature (panels (a) and (b)) and atmospheric density (panels (c) and (d)) profiles provided by the MCD database and for two different locations: 1. A Martian latitude $\phi = -90^\circ$ and $L_s = 90^\circ$ (northern summer/southern winter); and 2. A latitude $\phi = 60^\circ$ and $L_s = 270^\circ$ (northern winter/southern winter). Figure A7 illustrates the temporal and latitudinal variability of the relative mass influx for the OCCs and three orbital positions. Figure A8 presents the diurnal variability of the injection rate profiles for the OCCs and three meteoric metals: Na (left-hand panels), Mg (middle panels), and Al (right-hand panels). As discussed in Section 3.3, Figure A9 shows that refractory metals, such as Al, are released more efficiently at the dawn terminator in equatorial and mid-latitudes where small and fast particles exhibit a dominant contribution. Finally, Figure A10 shows the normalized mass histogram for the Earth atmosphere over the mass range considered by the Long

Duration Exposure Facility (LDEF, yellow) and the Dynamical Model of the Zodiacal Cloud for the Jupiter-family comets constrained with three different observations: SAAMER (orange), the Planck spacecraft (green), and the infrared Astronomical Satellite (IRAS, purple). This Figure will be discussed in detail in Appendix A.1.1.

Table A1 lists the elemental atomic abundances normalized to Si for a CI-chondrite composition (Lodders & Fegley 2011). Table A2 shows the surface area of the latitudinal bands in the Northern Hemisphere, in m^2 , assuming a fixed latitudinal bin of $\Delta\phi = 5^\circ$ and a volumetric mean radius for Mars of 3389.5 km .

A.1. Uncertainties of the CABMOD-MIF Model

A.1.1. Uncertainties of the DMZC Model

The DMZC model—and the MIF—provides a complete description of the size and velocity distributions based on the observations of the so-called apparent meteor sporadic sources as seen from a planetocentric frame of reference (Brown & Jones 1995; Campbell-Brown 2008; Janches et al. 2020) and, as discussed in Section 2.3, the knowledge of the combined effect of both distributions is necessary to assess accurately the peak ablation altitude of meteoric metals and the overall

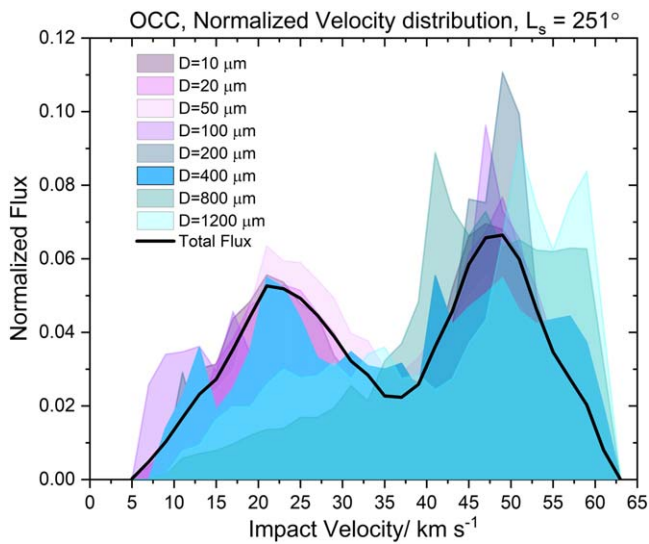


Figure A3. Normalized velocity distributions in Mars' orbit for the OCCs at perihelion ($L_s = 251^\circ$). The color profiles show the results for all those diameters modeled by both the DMZC and the MIF. The solid-black line also represents the normalized overall flux for each meteoroid population as a function of the impact velocity. Note that both the profiles of the velocity distributions for the different particle sizes and the overall flux are normalized to an area equal to unity.

Table A1

Elemental Atomic Abundances Normalized to Silicon and Oxide Mass in wt% for CI Chondrites (Lodders & Fegley 2011)

Metal Oxide	Carbonaceous Ivuna (CI) ^a		
	Elemental Abundance ^c	Oxide Mass wt%	(Metal): (2.5 × Na)
SiO ₂	1	34.8	7.02
FeO (Silicate) ^b	0.60	25.1	4.21
Fe (Metal) ^b	0.27	8.6	1.89
MgO	1.03	24.0	7.23
CaO	0.060	2.0	0.42
Al ₂ O ₃	0.083	2.4	0.58
TiO ₂	2.5×10^{-3}	0.11	0.017
Na ₂ O	0.057	1.0	0.4
K ₂ O	3.7×10^{-3}	0.10	0.026
Ni	0.048	1.6	0.34
P ₂ O ₅	8.2×10^{-3}	0.34	0.057
Mass fraction (silicate) ^b		0.90	
Mass fraction (metal) ^b		0.10	

Notes. The third column shows the metal ratios relative to Na, assuming an average enrichment of 2.5. The partition of Fe between the silicate phase and Fe–Ni metal grains and FeS domains is determined from Jarosewich (1990).

^a Lodders & Fegley (2011).

^b The distribution of Fe between silicate and FeNi metal phases is given by Jarosewich (1990).

^c Elemental abundances are given relative to Si.

ablation efficiency (see Figures 7 and 8). In this respect, the size distribution in the DMZC model is essentially characterized by the SFD (see Equation (1) in Section 2.1), and several measurements of the differential size index, σ , at 1 au suggest that this parameter is between $\sigma = 4.08 \pm 0.01$, based on a decade of meteor observations from the Southern Argentina Agile Meteor Radar (SAAMER; Janches et al. 2019), and

Table A2

Surface Area of the Latitudinal Bands in the Northern Hemisphere, $A_{\partial\phi}(\phi)$, in m², Assuming a Fixed Latitudinal Bin of $\Delta\phi = 5^\circ$ and a Volumetric Mean Radius for Mars of 3389.5 km

Latitudinal Band $\partial(\Delta\phi = 5^\circ)$	Surface Area of the Latitudinal Band ^a , $A_{\partial\phi}(\phi)$, in m ²
90°	2.7525×10^{11}
85°	5.4946×10^{11}
80°	1.0947×10^{12}
75°	1.6317×10^{12}
70°	2.1562×10^{12}
65°	2.6643×10^{12}
60°	3.1521×10^{12}
55°	3.6160×10^{12}
50°	4.0523×10^{12}
45°	4.4578×10^{12}
40°	4.8294×10^{12}
35°	5.1642×10^{12}
30°	5.4597×10^{12}
25°	5.7136×10^{12}
20°	5.9241×10^{12}
15°	6.0895×10^{12}
10°	6.2085×10^{12}
5°	6.2803×10^{12}
0°	6.3043×10^{12}
Total surface area of Mars = $2 \times (\sum A_{\partial\phi}(\phi))$	1.4437×10^{14}

Note.

^a The surface area of a latitudinal band centered at latitude ϕ is expressed by $A_{\partial\phi}(\phi) = \int_0^{2\pi} \int_{\phi_1}^{\phi_2} r^2 \cos \phi d\phi d\Gamma = 2\pi r^2 [\sin \phi_2 - \sin \phi_1]$, where $\partial\phi = \phi_2 - \phi_1$.

$\sigma = 5.05$ (Grün et al. 1985) for $D < 2000 \mu\text{m}$. Figure A10 exemplifies the dependence of the normalized mass influx of the incoming bulk of the JFCs predicted by the DMZC model with different values of σ , and compared with measurements of the LDEF spacecraft at Earth's orbit (Love & Brownlee 1993). According to Figure A10, the mass influx is preferentially shifted to larger size ranges with lower values of σ . Consequently, larger median sizes in the mass influx distribution lead to both lower altitudes of the ablation peaks of meteoric metals (Figure 7) and higher overall ablation efficiencies (Figure 8). The values of the differential size indices considered in the present study— $\sigma = 4.6$ (JFCs), $\sigma = 4$ (ASTs), and $\sigma = 4$ (HTCs)—were primarily used to explain the fluxes of cosmic spherules at the Earth's South Pole water well (Taylor et al. 1998) and the vertical fluxes of Na and Fe measured by LiDAR observations at Earth (Gardner et al. 2014). However, in a future work, they will be reassessed assuming SAAMER observations (Janches et al. 2019), and recent estimates of the annual accretion rates of both spherules and unmelted micrometeorites at the CONCORDIA Station located at Dome C (Antarctica; Rojas et al. 2021).

Regarding the velocity distribution, radar observations at Earth indicate that average geocentric speeds are highest for the retrograde meteoroids in the apex direction and lowest near the antiapex, whereas slow meteoroids in prograde orbits are mainly located at the helion and antihelion directions (Janches et al. 2017, 2019, 2020). Over the last several decades, given the lack of direct measurements of impact velocities of meteoroids in orbits far from Earth, several authors have extrapolated our current knowledge of the velocity distribution around Earth's orbit to terrestrial bodies in the inner solar

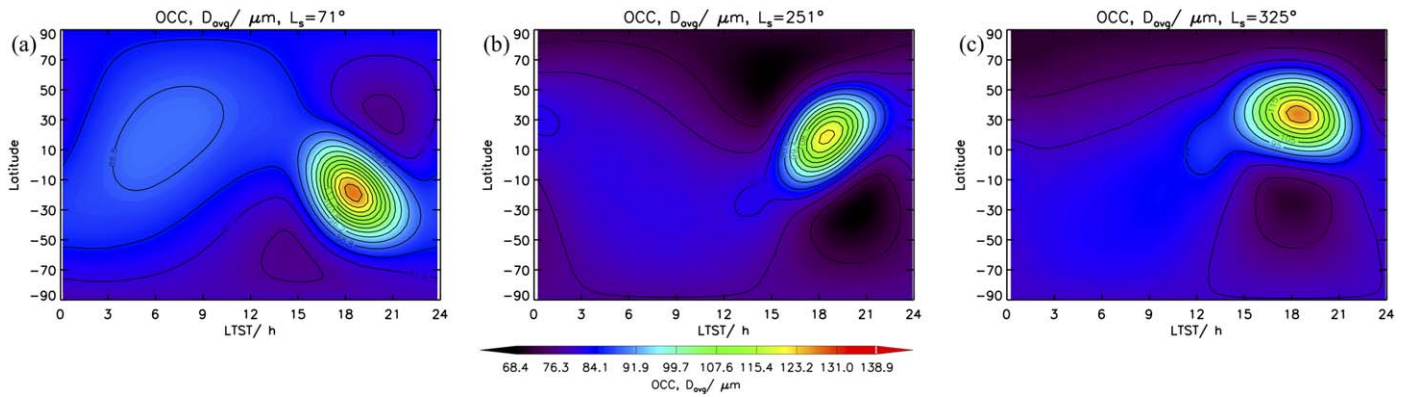


Figure A4. Diurnal variability of the average diameter distribution (in microns) of meteoroids into the Martian atmosphere determined by the MIF model for the OCCs and three orbital positions: aphelion ($L_s = 71^\circ$, (a)), perihelion ($L_s = 251^\circ$, (b)), and first crossing of the ecliptic plane ($L_s = 325^\circ$, (c)). These distributions are represented as a function of the Local True Solar Time and the latitude at Mars. Note that the maximum diurnal size for the OCCs appears at $L_s = 244^\circ$.

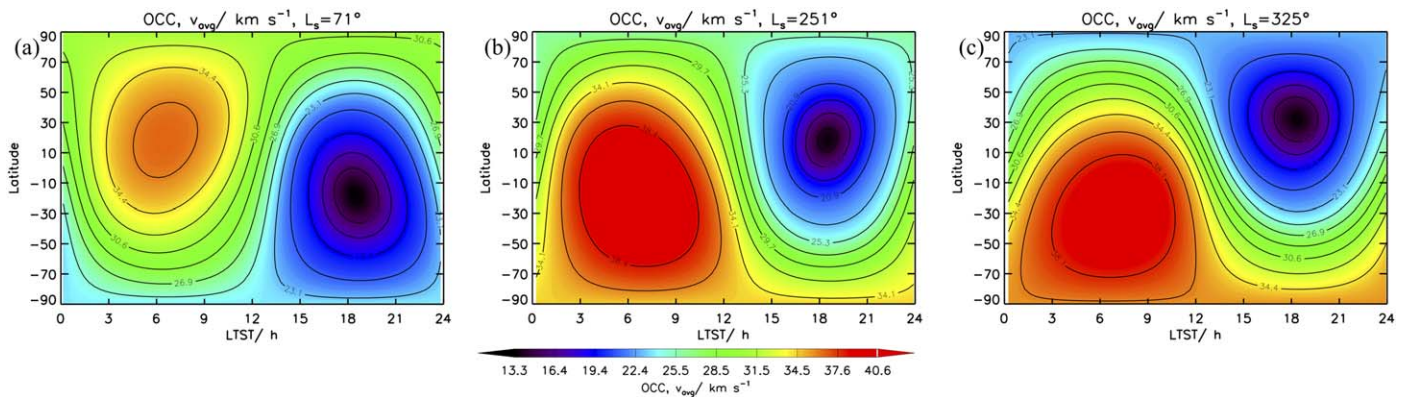


Figure A5. Diurnal variability of the average velocity distribution (in kilometers per second) of meteoroids into the Martian atmosphere modeled by the MIF model for the OCCs and three orbital positions: aphelion ($L_s = 71^\circ$, (a)), perihelion ($L_s = 251^\circ$, (b)), and first crossing of the ecliptic plane ($L_s = 325^\circ$, (c)). These distributions are represented as a function of the Local True Solar Time and the latitude at Mars.

system (Ma et al. 2014; Borin et al. 2017; Pokorný et al. 2018, 2019). In the present study, as shown in Figures 3 and A2, the DMZC model for Mars produces radiant maps of the velocity distributions, with meteoroids in prograde and retrograde orbits populating equivalent apparent sources to those observed at Earth.

A.1.2. Uncertainties of the CABMOD Model

Regarding the CABMOD model, there are three sources of uncertainty: (1) the initial chemical composition of the particle bulk; (2) the description of the mineralogical structure in the meteoroid; and (3) the potential alteration of the mechanical properties during the atmospheric entry.

As a reference, the CABMOD model considers the elemental atomic abundances of CI chondrites for all of the chemical constituents (see Table A1; Lodders & Fegley 2011); that is, particles are mineralogically and compositionally similar to the primitive nebular condensate. Nevertheless, after formation of chondritic bodies through accretion in the early solar system, meteoroids undergo space weathering, altering their physical and chemical properties and mineralogy. In this way, carbonaceous chondrites are associated with transitional objects with a significant abundance of hydrated minerals (Trigo-Rodríguez 2015; Koschny et al. 2019), whereas ordinary chondrites have suffered a significant chemical and thermal processing to produce

particles with higher strength, less bulk porosity, and higher density (Trigo-Rodríguez & Blum 2009; Moyano-Camero et al. 2017). Regarding the mineralogical analysis of recovered micrometeorites, Taylor et al. (2012) reported that about 75% of cosmic spherules are estimated to be CI- and CM-like fine-grained aggregates containing a variety of anhydrous and hydrated silicate minerals, along with troilite (FeS) and Fe–Ni alloy. Hydrated silicates experience chemical and mineralogical reactions above 900 K (Greshake et al. 1998), and the melting points of anhydrous minerals span a range of temperature between ~ 1400 and ~ 2200 K, controlling to some extent the ablation characteristics of the incident dust flux. As discussed in Section 2.3, the CABMOD model includes a multiphase treatment to account for the ablation rates from both the silicate and Fe–Ni metal phases in IDPs. In the case of the silicate bulk, CABMOD assumes an ideal anhydrous single-mineral phase using the MAGMA thermodynamic module to estimate the vapor pressures of meteoric metals (see Section 2.3; Fegley & Cameron 1987; Schaefer & Fegley 2004), and removing any chemical and mineralogical alteration produced by the presence of aqueously processed minerals. The Meteor Ablation Simulator (MASI), a laboratory experimental setup developed at the University of Leeds, has been used to refine and validate the CABMOD model with experimental measurements of the evaporating metals from meteoric samples by laser-induced fluorescence (Bones et al. 2016; Gómez-Martín et al. 2017).

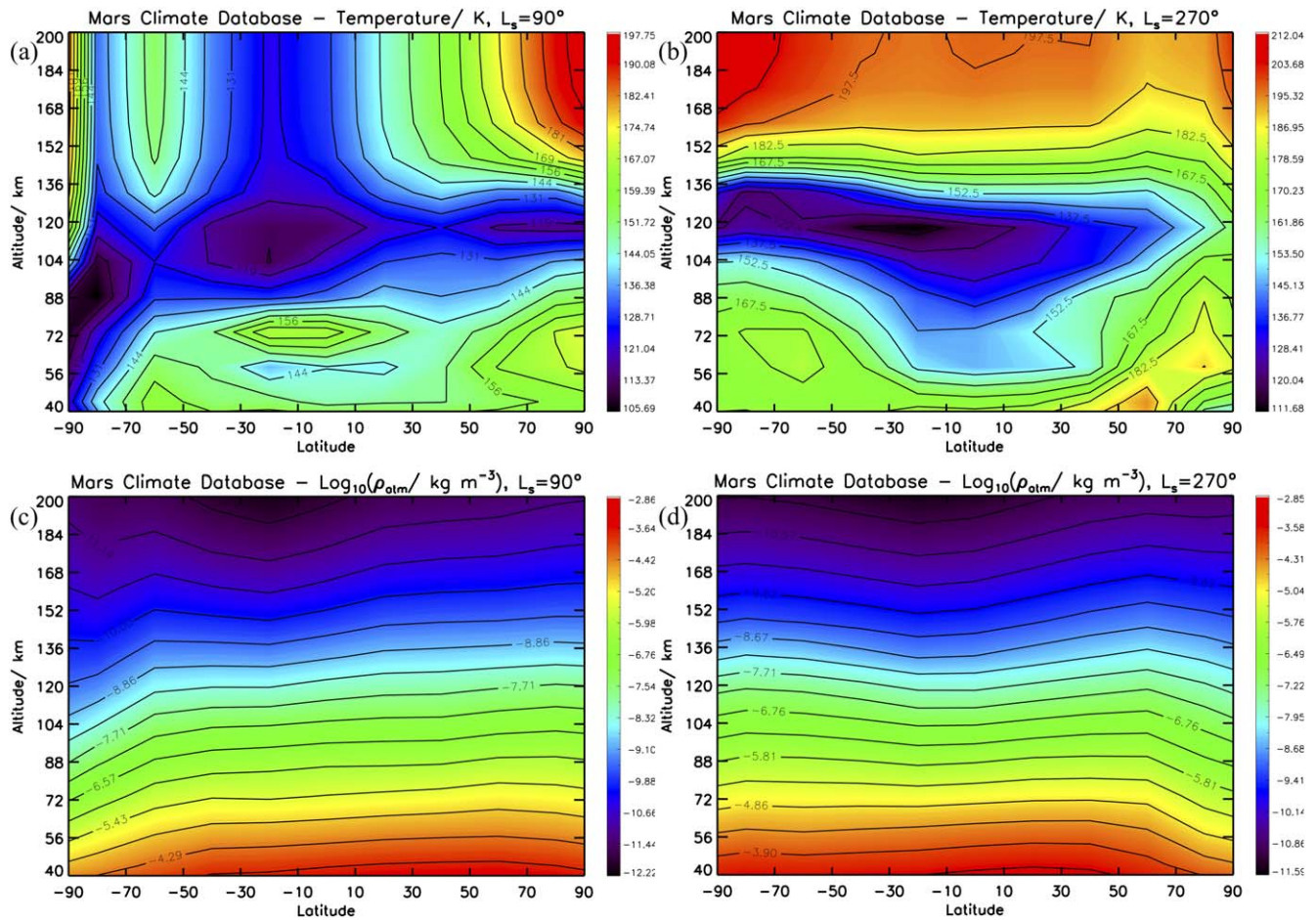


Figure A6. Temperature (panels (a) and (b)) and atmospheric density (panels (c) and (d)) profiles for two orbital positions: $L_s = 90^\circ$ (northern summer/southern winter) and $L_s = 270^\circ$ (northern winter/southern summer) as a function of the altitude and the latitude at Mars. These data correspond to the MCD.

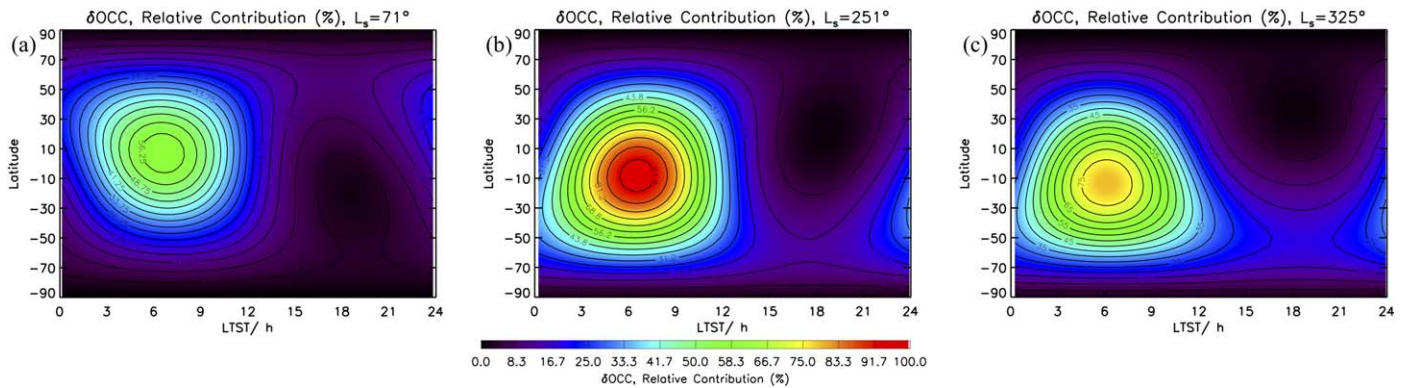


Figure A7. Diurnal variability of the relative mass influx of meteors into the Martian atmosphere determined by the MIF model for the OCCs and three orbital positions: aphelion ($L_s = 71^\circ$, (a)), perihelion ($L_s = 251^\circ$, (b)), and first crossing of the ecliptic plane ($L_s = 325^\circ$, (c)).

According to the MASI experimental results, the CABMOD model reproduces satisfactorily the measured peak ablation pulses and the relative ablated fractions from silicate—Fe, Na, P, and Ca—and metal Fe–Ni phases (Gómez-Martín et al. 2017; Bones et al. 2019; Carrillo-Sánchez et al. 2020a, 2020b), indicating that the assumption of an ideal and anhydrous-silicate molten bulk in the CABMOD model is a reasonable approximation for most of the meteoric ablated metals. Nonetheless, even though the CABMOD model reproduces most of the ablation features of the Mg pulses measured by the MASI (Bones et al. 2018), it does not

completely capture the width of the Mg ablation profiles, because of the presence of different mineral phases, mainly hydrous Mg-silicates, which melt inhomogeneously. Therefore, the MASI results suggest that the overall injection rates of Mg estimated by the CABMOD-MIF model should be slightly broader (see Figure 4 in Bones et al. 2018).

In terms of composition, meteoroids entering in a planetary atmosphere may exhibit relative enrichment or depletion of the elemental atomic abundances compared to primitive CI chondrites, which may have a significant impact on the

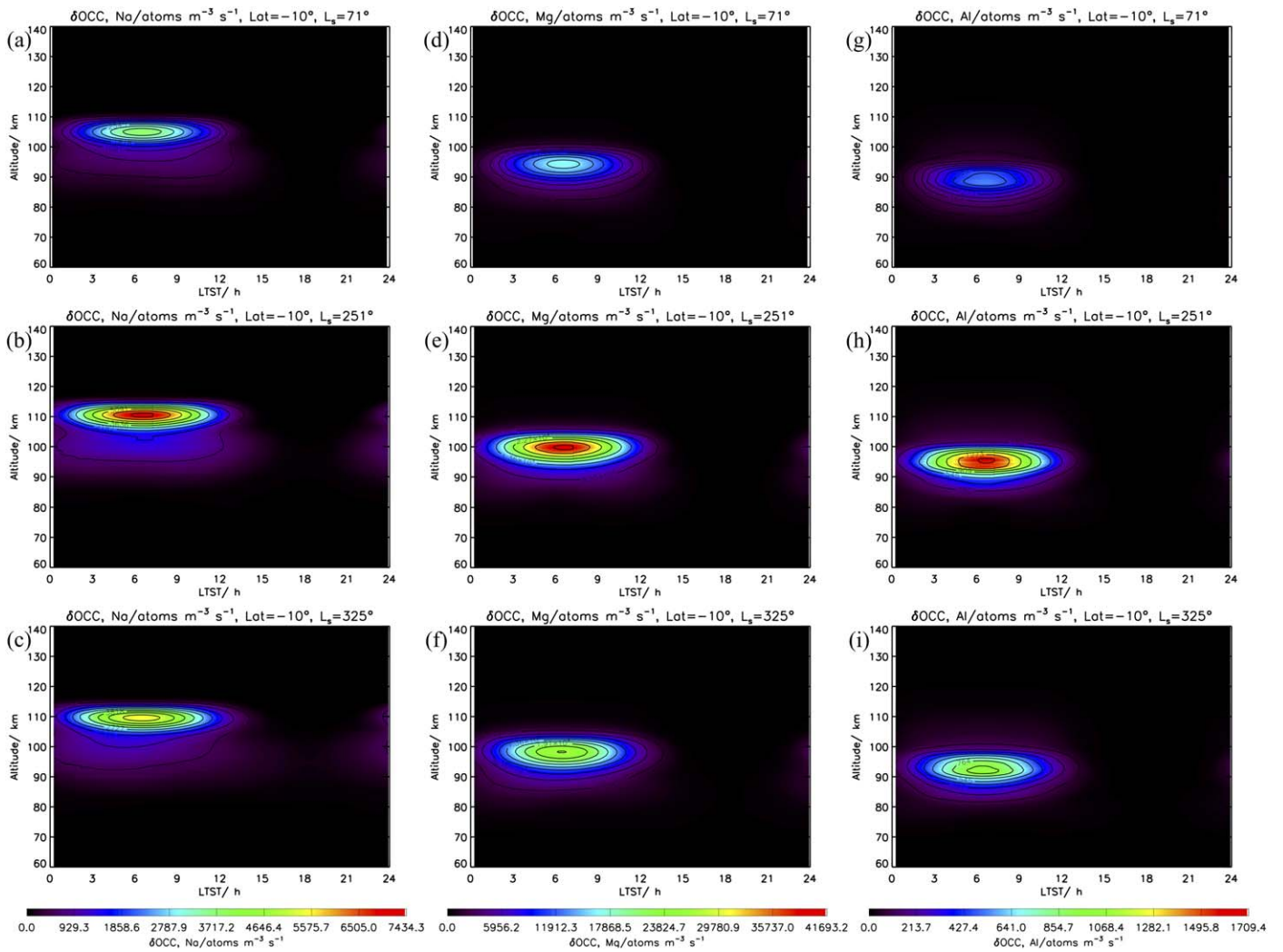


Figure A8. Diurnal variability of the injection rates (in $\text{atoms m}^{-3} \text{s}^{-1}$) of Na (a, b, and c), Mg (d, e, and f), and Al (g, h, and i) estimated by the CABMOD-MIF model for the OCCs and three orbital positions: aphelion ($L_s = 71^\circ$, top panels), perihelion ($L_s = 251^\circ$, middle panels), and first crossing of the ecliptic plane ($L_s = 325^\circ$, bottom panels). The maximum ablation rates of the three metals appear at perihelion and for a latitude of -10° . Note that the color scales are different for each meteoric metal.

injection rates in some ablated meteoric metal. For example, meteoroids of cometary origin are normally enriched in Na by a factor between ~ 2.0 —from the Stardust mission to comet 81P/Wild 2 and meteor spectroscopic analysis (Trigo-Rodríguez & Llorca 2007; Gainsforth et al. 2015)—and 4.8 ± 3.7 —from the Rosetta mission to 67P/Churyumov-Gerasimenko (Hilchenbach et al. 2016). In contrast, fragments from asteroids, especially from S-type asteroids, have been significantly altered by thermal metamorphism and mineralogical modifications leading to a depletion in Na by a factor of ~ 1.4 (Borovička et al. 2005). In this study, the CABMOD-MIF model assumes that the cometary particles are enriched in Na by an average factor of 2.5, while particles from asteroidal origin preserve their initial CI atomic abundances (Carrillo-Sánchez et al. 2016).

Finally, IDPs may experience, during atmospheric entry, a significant alteration of their mechanical properties due to both the pyrolysis of the organic constituents between 700 and 800 K (Bones et al. 2022) and sudden vesicle formation on hydrated micrometeoroids after exceeding the solidus temperature of 1414 K (Ghiorso 1985; Genge 2017). On the one hand, Bones et al. (2022)

measured the pyrolysis kinetics of meteoritic samples by mass spectrometric detection of CO_2 and SO_2 at temperatures between 625 and 1300 K, and subsequent atomic force microscopy of the residual meteoritic particles, indicating that these residual samples become more brittle and slightly harder after organic pyrolysis. Moreover, Bones et al. (2022) concluded that most cosmic dust particles ($< 100 \mu\text{m}$) will not fragment during the entry into the atmosphere as a result of organic pyrolysis. On the other hand, vesicle formation on hydrated particles leads to a sudden expansion of around 70% in volume and a decrease in bulk density above the solidus temperature of 1414 K (Genge 2017), giving rise to a particle deceleration along with a decrease of the peak temperature. Numerical simulations suggest that the magnitude of the peak temperature decrease is largest ($> 100 \text{ K}$) for particles that partially melt, while the temperature decrease is less marked ($< 50 \text{ K}$) for those particles that exceed the melting temperature. Thereupon, while vesicular parachuting increases the range of initial particle sizes that survive as unmelted micrometeorites or cosmic spherules, a slight decrease of the peak temperature in fully melted particles (see Figure 2 in Genge 2017) would not significantly reduce the injection rates of ablated metals, and, in terms of ablation, this effect

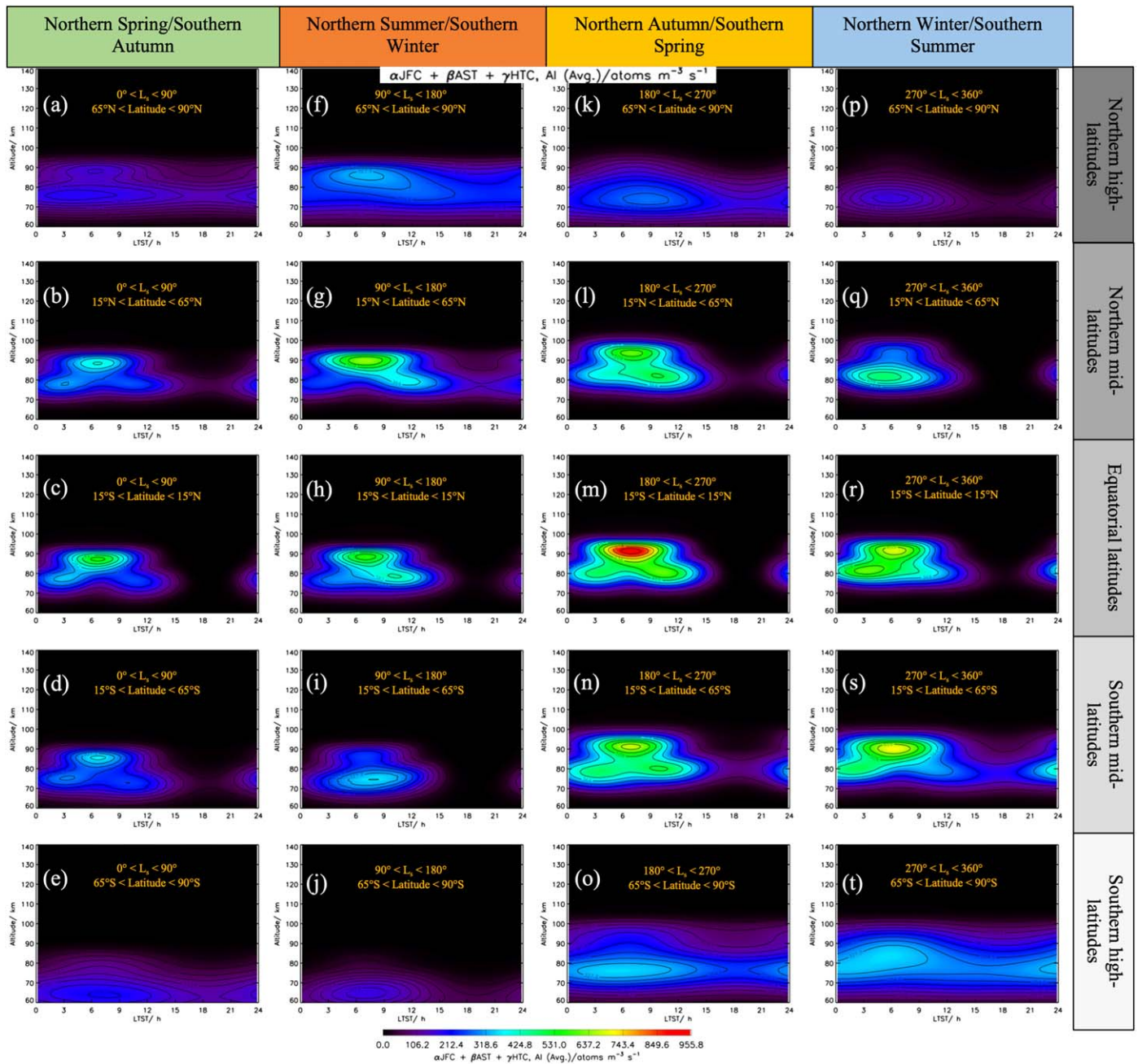


Figure A9. Average diurnal variability of the total injection rates (in atoms $\text{m}^{-3} \text{s}^{-1}$) of Al estimated by the CABMOD-MIF model at northern high latitudes ($65^\circ < \phi < 90^\circ$, panels (a), (f), (k), and (p)), northern mid-latitudes ($15^\circ < \phi < 65^\circ$, panels (b), (g), (l), and (q)), equatorial latitudes ($-15^\circ < \phi < 15^\circ$, panels (c), (h), (m), and (r)), southern mid-latitudes ($-15^\circ < \phi < -65^\circ$, panels (d), (i), (n), and (s)), and southern high latitudes ($-65^\circ < \phi < -90^\circ$, panels (e), (j), (o), and (t)). The left panels represent the average rates between $L_s = 0^\circ$ (northern spring/southern fall) and $L_s = 90^\circ$ (northern summer/southern winter). Panels in the second column show the average rates between $L_s = 90^\circ$ (northern summer/southern winter) and $L_s = 180^\circ$ (northern fall/southern spring). Panels in the third column represent the average rates between $L_s = 180^\circ$ (northern fall/southern spring) and $L_s = 270^\circ$ (northern winter/southern summer). The right panels show the average rates between $L_s = 270^\circ$ (northern winter/southern summer) and $L_s = 360^\circ$ (northern spring/southern fall).

is considered negligible in the present study. Notwithstanding, future CABMOD simulations will include both the pyrolysis kinetics of organics in the upper atmosphere and the assessment of vesicular parachuting of meteors.

A.1.3. Uncertainties of the Mars-LMD Model

As discussed in Section 2.3, the altitude of the ablation peak of meteoric metals and the overall ablation efficiency depend to some extent on changes in the atmospheric density structure. In

the present study, the CABMOD model simulates the atmospheric density profiles using the MCD database (Lewis et al. 1999), which is derived from the Mars-LMD model. However, observations with the Mars Express ultraviolet spectrometer Spectroscopy for Investigation of Characteristics of the Atmosphere of Mars (SPICAM; Forget et al. 2009) and the Mars Climate Sounder (Navarro et al. 2017) for the middle atmosphere have demonstrated that data assimilation at Mars is found to be distinctively challenging due to the difficulty of capturing global atmospheric thermal tides. Accordingly, Forget et al. (2009)

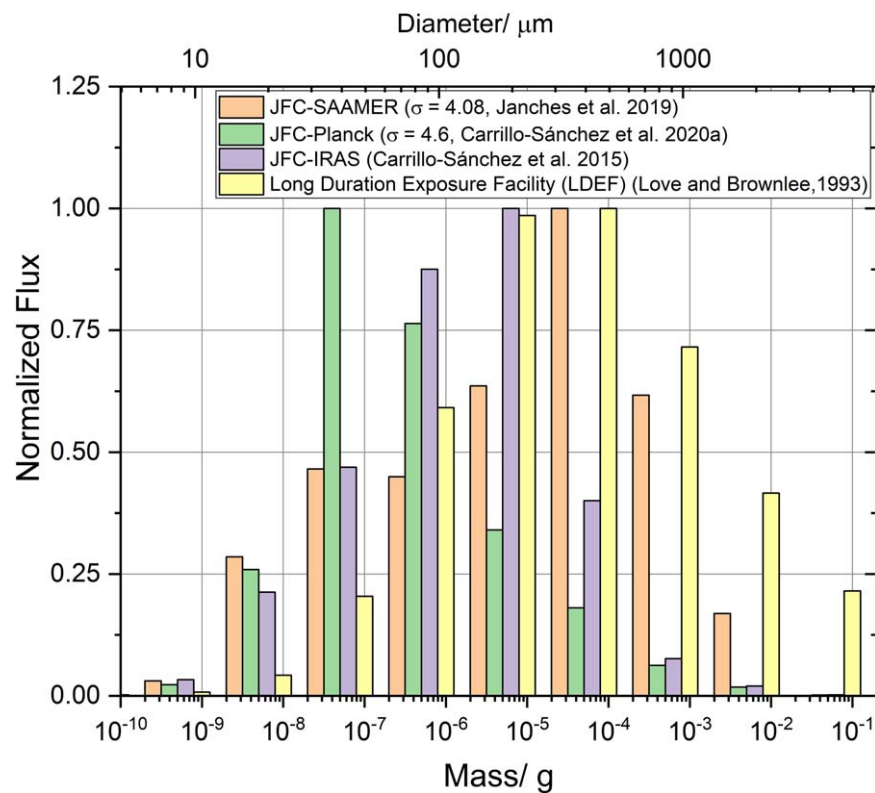


Figure A10. Histogram displaying the normalized mass influx rate into Earth's atmosphere over the mass range considered by the LDEF spacecraft (yellow) and the DMZC for the JFCs constrained with three different observations: SAAMER (orange), Planck satellite (green), and IRAS satellite (purple).


concluded that: (1) the atmospheric densities exhibit marked seasonal fluctuations as a result of the dust content, which controls the atmospheric temperature; and (2) the LMD-Mars model overestimated the atmospheric temperature observed by SPICAM between 80 and 100 km by up to 30 K. More recently, MAVEN/IUVS stellar occultation observations measured temperature profiles and CO_2 , O_2 , and O_3 number densities distributions covering seven orders of magnitude in pressure—from 2×10^1 to 4×10^{-7} Pa—and latitudes from -80° and 75° (Gröller et al. 2018). The comparison between MAVEN/IUVS observations and the current Mars-LMD model shows that simulations can capture the seasonal and vertical structures of the temperature between 1 and 10^{-3} Pa (Gröller et al. 2018), covering the typical ablation pressure levels at Mars (see Figure 16). However, the Mars-LMD simulation may underestimate, by up to 30 K, periodic perturbations of the temperature profile observed by the MAVEN/IUVS between the pressure levels 10^{-1} and 10^{-2} Pa, likely due to the presence of thermal tides and waves, which are challenging to model. Future missions at Mars will help to further constrain and validate the Mars-LMD model (Almatroushi et al. 2021) and, hence, to reduce modeling uncertainties.


ORCID iDs

Juan Diego Carrillo-Sánchez  <https://orcid.org/0000-0001-8230-4048>

Diego Janches  <https://orcid.org/0000-0001-8615-5166>

John M. C. Plane  <https://orcid.org/0000-0003-3648-6893>

Petr Pokorný  <https://orcid.org/0000-0002-5667-9337>

Menelaos Sarantos  <https://orcid.org/0000-0003-0728-2971>

Matteo M. J. Crismani  <https://orcid.org/0000-0003-3127-2466>

Wuhu Feng  <https://orcid.org/0000-0002-9907-9120>

Daniel R. Marsh  <https://orcid.org/0000-0001-6699-494X>

References

- Acton, C. H. 1996, *P&SS*, 44, 65
- Ade, P. A. R., Aghanim, N., Armitage-Caplan, C., et al. 2014, *A&A*, 571, A14
- Almatroushi, H., AlMazmi, H., AlMheiri, N., et al. 2021, *SSRv*, 217, 89
- Andersson, L., Weber, T. D., Malaspina, D., et al. 2015, *Sci*, 350, 0398
- Banya, S. 1993, *ISIJ International*, 33, 2
- Benna, M., Mahaffy, P. R., Grebowsky, J. M., et al. 2015, *GeoRL*, 42, 4670
- Bolton, S. J., Stevenson, D., Connerney, J. E. P., et al. 2017, *SSRv*, 213, 5
- Bones, D. L., Carrillo Sánchez, J. D., Connell, S. D. A., et al. 2022, *E&SS*, 9, e01884
- Bones, D. L., Carrillo-Sánchez, J. D., Kulak, A. N., & Plane, J. M. C. 2019, *P&SS*, 179, 104725
- Bones, D. L., Gómez Martín, J. C., Carrillo Sánchez, J. D., Dobson, A. J., & Plane, J. M. C. 2018, *GeoRL*, 45, 07765
- Bones, D. L., Gómez Martín, J. C., Empson, C. J., et al. 2016, *RSci*, 87, 094504
- Borin, P., Cremonese, G., Marzari, F., & Lucchetti, A. 2017, *A&A*, 605, A94
- Borovička, J., Koten, P., Spurný, P., Boček, J., & Štork, R. 2005, *Icar*, 174, 15
- Brown, P., & Jones, J. 1995, *EM&P*, 68, 223
- Brown, P., Weryk, R. J., Wong, D. K., & Jones, J. W. 2008, *Icar*, 195, 317
- Campbell-Brown, M. D. 2008, in *Advances in Meteoroid and Meteor Science*, ed. J. M. Trigo-Rodríguez et al. (New York: Springer), 79
- Carrillo-Sánchez, J. D., Bones, D. L., Douglas, K. M., et al. 2020b, *P&SS*, 187, 104926
- Carrillo-Sánchez, J. D., Gómez-Martín, J. C., Bones, D. L., et al. 2020a, *Icar*, 335, 113395
- Carrillo-Sánchez, J. D., Nesvorný, D., Pokorný, P., Janches, D., & Plane, J. M. C. 2016, *GeoRL*, 43, 11979
- Carrillo-Sánchez, J. D., Plane, J. M. C., Feng, W., Nesvorný, D., & Janches, D. 2015, *GeoRL*, 42, 6518
- Ceplecha, Z., Borovička, J., Elford, W. G., et al. 1998, *SSRv*, 84, 327
- Chase, M. W., Davies, C. A., Downey, J. R., Jr, et al. 1985, *Journal Physical and Chemical Reference Data*, 14, 535
- Conard, B. R., McAneny, T. B., & Sridhar, R. 1978, *MTB*, 9, 463
- Connerney, J. E. P., Benn, M., Bjarno, J. B., et al. 2017, *SSRv*, 213, 39
- Crismani, M. M. J., Schneider, N. M., Evans, J. S., et al. 2018, *JGRE*, 123, 2613
- Crismani, M. M. J., Schneider, N. M., Plane, J. M. C., et al. 2017, *NatGe*, 10, 401

- Crismani, M. M. J., Tyo, R. M., Schneider, N., et al. 2022, *JGRE*, Submitted
- Evatt, G. W., Smedley, A. R. D., Joy, K. H., et al. 2020, *Geo*, **48**, 683
- Fegley, B. J., & Cameron, A. G. W. 1987, *E&PSL*, **82**, 207
- Flynn, G. J., Consolmagno, G. J., Brown, P., & Macke, R. J. 2018, *ChEG*, **78**, 269
- Forget, F., Montmessin, F., Bertaux, J.-F., et al. 2009, *JGRE*, **114**, E01004
- Gainsforth, Z., Butterworth, A. L., Stodolna, J., et al. 2015, *M&PS*, **50**, 976
- Gardner, C. S., Liu, A. Z., Marsh, D. R., Feng, W. H., & Plane, J. M. C. 2014, *JGRA*, **119**, 7870
- Genge, M. J. 2017, *GeoRL*, **44**, 1679
- Ghiorso, M. S. 1985, *CoMP*, **90**, 107
- Gómez-Martín, J. C., Bones, D. L., Carrillo-Sánchez, J. D., et al. 2017, *ApJ*, **836**, 212
- Grebowsky, J. M., Benna, M., Plane, J. M. C., et al. 2017, *GeoRL*, **44**, 3066
- Grebowsky, J. M., Goldberg, R. A., & Pesnell, W. D. 1998, *JASTP*, **60**, 607
- Greshake, A., Kloeck, W., Arndt, P., et al. 1998, *M&PS*, **33**, 267
- Gröller, H., Montmessin, F., Yelle, R. V., et al. 2018, *JGRE*, **123**, 1449
- Grün, E., Zook, H. A., Fechtig, H., & Giese, R. H. 1985, *Icar*, **62**, 244
- Hilchenbach, M., Kissel, J., Langevin, Y., et al. 2016, *ApJL*, **816**, L32
- Hutchinson, R. 2004, *Meteorites: A Petrologic, Chemical and Isotopic Synthesis* (Cambridge: Cambridge Univ. Press)
- Janches, D., Brunini, C., & Hormaechea, J. L. 2019, *AJ*, **157**, 240
- Janches, D., Bruzzone, J. S., Pokorný, P., Carrillo-Sánchez, J. D., & Sarantos, M. 2020, *PSJ*, **1**, 59
- Janches, D., Swarnalingam, N., Carrillo-Sánchez, J. D., et al. 2017, *ApJ*, **843**, 1
- Jarosewich, E. 1990, *Metic*, **25**, 323
- Jorgensen, J. L., Benn, M., Connerney, J. E. P., et al. 2021, *JGRE*, **126**, e06509
- Keller, L. P., & Flynn, G. J. 2022, *NatAs*, **6**, 731
- Kopp, E. 1997, *JGR*, **102**, 9667
- Koschny, D., Soja, R. H., Engrand, C., et al. 2019, *SSRv*, **215**, 34
- Lewis, S. R., Collins, M., Read, P. L., et al. 1999, *JGR*, **104**, 24177
- Lodders, K., & Fegley, B. J. 2011, *Chemistry of the Solar System*. The Royal Society of Chemistry (Cambridge: Cambridge Univ. Press)
- Love, S. G., & Brownlee, D. E. 1993, *Sci*, **262**, 550
- Ma, C., Beckett, J. R., & Rossman, G. R. 2014, *AmMin*, **99**, 198
- Millour, E., & Forget, F. 2008, Mars Climate Database v4.3 Detailed Design Document, ESTEC Contract 11369/95/NL/JG, http://www-mars.lmd.jussieu.fr/mars/info_web/user_manual_4.3.pdf
- Molina-Cuberos, G. J., Witasse, O., Lebreton, J. P., Rodrigo, R., & Lopez-Moreno, J. J. 2003, *P&SS*, **51**, 239
- Moyano-Camero, C. E., Trigo-Rodríguez, J. M., & Benito, M. I. 2017, *M&PS*, **52**, 1030
- Navarro, T., Forget, F., Millour, E., et al. 2017, *E&SS*, **4**, 690
- Nesvorný, D., Janches, D., Vokrouhlický, D., et al. 2011, *ApJ*, **743**, 129
- Nesvorný, D., Jenniskens, P., Levison, H. F., et al. 2010, *ApJ*, **713**, 816
- Pesnell, W. D., & Grebowsky, J. M. 2000, *JGR*, **105**, 1695
- Plane, J. M. C. 2003, *ChRv*, **103**, 4963
- Plane, J. M. C., Carrillo-Sánchez, J. D., Mangan, T. P., et al. 2018c, *JGRE*, **123**, 695
- Plane, J. M. C., Feng, W., & Dawkins, E. C. M. 2015, *ChRv*, **115**, 4497
- Plane, J. M. C., Feng, W. H., Martin, J. C. G., Gerding, M., & Raizada, S. 2018b, *ACP*, **18**, 14799
- Plane, J. M. C., Flynn, G. J., Määttänen, A., et al. 2018a, *SSRv*, **214**, 23
- Pokorný, P., Janches, D., Sarantos, M., et al. 2019, *JGRE*, **124**, 752
- Pokorný, P., Mazarico, E., & Schorghofer, N. 2021, *PSJ*, **2**, 85
- Pokorný, P., Sarantos, M., & Janches, D. 2017, *ApJ*, **842**, L17
- Pokorný, P., Sarantos, M., & Janches, D. 2018, *ApJ*, **863**, 31
- Pokorný, P., Sarantos, M., Janches, D., & Mazarico, E. 2020, *ApJ*, **894**, 114
- Pokorný, P., Szalay, J. R., Horányi, M., & Kuchner, M. J. 2022, *PSJ*, **3**, 14
- Pokorný, P., Vokrouhlický, D., Nesvorný, D., Campbell-Brown, M., & Brown, P. 2014, *ApJ*, **789**, 25
- Poppe, A. R. 2016, *Icar*, **264**, 369
- Poppe, A. R., Lisse, C. M., Piquette, M., et al. 2019, *ApJL*, **881**, L12
- Robertson, D., Pokorný, P., Granvik, M., Wheeler, L., & Rumpf, C. 2021, *PSJ*, **2**, 88
- Rojas, J., Duprat, J., Engrand, C., et al. 2021, *E&PSL*, **560**, 116794
- Rowan-Robinson, M., & May, B. 2013, *MNRAS*, **429**, 2894
- Schaefer, L., & Fegley, B. 2004, *Icar*, **169**, 216
- Schneider, N. M., Deighan, J. I., Stewart, A. I. F., et al. 2015, *GeoRL*, **42**, 4755
- Steel, D. I., & Elford, W. G. 1986, *MNRAS*, **218**, 185
- Swartzendruber, L. J., Itkin, V. P., & Alcock, C. B. 1991, *Journal of Phase Equilibria*, **12**, 288
- Szalay, J. R., Pokorný, P., Horányi, M., et al. 2019, *P&SS*, **165**, 194
- Taylor, S., Lever, J. H., & Harvey, R. P. 1998, *Natur*, **392**, 899
- Taylor, S., Matrajt, G., & Guan, Y. B. 2012, *M&PS*, **47**, 550
- Trigo-Rodríguez, J. M. 2015, in *Planetary Mineralogy*, ed. M. R. Lee & H. Leroux (European Mineralogical Union)
- Trigo-Rodríguez, J. M., & Blum, J. 2009, *PASA*, **26**, 289
- Trigo-Rodríguez, J. M., & Llorca, J. 2007, *AdSpR*, **39**, 517
- Vondrak, T., Plane, J. M. C., Broadley, S., & Janches, D. 2008, *ACP*, **8**, 7015
- Whalley, C. L., & Plane, J. M. C. 2010, *FaDi*, **147**, 349
- Yang, H. G., & Ishiguro, M. 2015, *ApJ*, **813**, 9
- Zook, H. A. 2001, in *Accretion of Extraterrestrial Matter Throughout Earth's History*, ed. B. Peucker-Ehrenbrink & B. Schmitz (Boston, MA: Springer), **75**